

Teemu Ruokokoski

## **A RADAR FRONT-END OF A PLANETARY ALTIMETER**

Thesis for the degree of Licentiate of Science in Technology submitted for inspection,  
Espoo, June 12, 2019.

Supervising professor

Professor Zachary Taylor

Thesis advisor

Professor Antti Räisänen

<b>Author</b> Teemu Ruokokoski	
<b>Title of thesis</b> A Radar Front-end of a Planetary Altimeter	
<b>Department</b> Electronics and nanoengineering	
<b>Field of research</b> Electrical Engineering	
<b>Supervising professor</b> Zachary Taylor	<b>Code of professorship</b> S-26
<b>Thesis advisor</b> Antti Räisänen	
<b>Thesis examiner</b> Pekka Pursula	
<b>Number of pages</b> 77	<b>Language</b> English
<b>Date of submission for examination</b> June 12, 2019	

### **Abstract**

The European Space Agency (ESA) is aiming for small landers in future planetary exploration missions. This imposes drastic design constraints on individual components in terms of size, mass and power. A reliable measurement of the ground distance by an altimeter is the key asset for the planetary descent and landing system. In the case of small landers, the size, mass and power consumption of the altimeter must be minimized as well.

Harp Technologies Ltd. was responsible for developing a radar front-end of a planetary altimeter. The main project objective was to analyse the most promising radar concept for ESA's exploration programme, and then design and bread-board the chosen concept.

A development of a frequency modulated continuous wave (FMCW) radar front-end for the frequency band 13.25 – 13.35 GHz is described in this Licentiate thesis. At first, a theoretical background for pulse and FMCW radars is presented. Based on the operational requirements, the FMCW radar concept is selected for the further development. The detailed design of the radar front-end is then described, and the performance of the manufactured breadboard is verified in laboratory conditions. The measured power consumption of the radar front-end is less than 2.5 W. The output frequency range is 13.28 – 13.389 GHz and the output power is approximately 14 dBm. The noise figure of the receiver is 6.5 dB. The performance of the realised radar altimeter is deemed satisfactory, and it has also sufficient improvement potential to be suitable for the next phase of the project (i.e. Engineering Model).

---

**Keywords:** radar, FMCW, altimeter

---

<b>Tekijä</b> Teemu Ruokokoski	
<b>Työn nimi</b> A Radar Front-end of a Planetary Altimeter	
<b>Laitos</b> Elektroniikka ja nanotekniikka	
<b>Tutkimusala</b> Sähkötekniikka	
<b>Työn valvoja</b> Zachary Taylor	<b>Koodi</b> S-26
<b>Työn ohjaaja</b> Antti Räisänen	
<b>Työn tarkastaja</b> Pekka Pursula	
<b>Sivumäärä</b> 77	<b>Kieli</b> englanti
<b>Lähetetty tarkastettavaksi</b> 12.06.2019	

## Tiivistelmä

Euroopan avaruusjärjestö (ESA) tähtää pieniin laskeutujiin tulevaisuuden planeetta-tutkimusohjelmissa. Tämä aiheuttaa merkittäviä suunnittelurajoituksia yksittäisten komponenttien koolle, massalle ja tehonkulutukselle. Luotettava maanpinnan etäisyyden mittaaminen korkeusmittarilla on planeettalaskeutumisjärjestelmän keskeinen voimavara. Pienten laskeutujien tapauksessa myös korkeusmittarin koko, massa ja tehonkulutus täytyy minimoida.

Harp Technologies Oy oli vastuussa planetaarisen korkeusmittarin tutkaetupään kehityksestä. Projektin päätavoite oli analysoida lupaavin tutkakonsepti ESAn tutkimusohjelmaa varten ja sitten suunnitella ja toteuttaa koekytkentämalli valitulle konseptille.

Tässä lisensiaatintyössä kuvaillaan taajuusmoduloidun jatkuvalähetteen (FMCW) tutkan etupään kehitys taajuusalueelle 13.25 – 13.35 GHz. Aluksi esitetään pulssi- ja FMCW-tutkien teoreettinen tausta. FMCW-tutkakonsepti valitaan jatkokehitykseen toimintavaatimusten perusteella. Tämän jälkeen tutkaetupään suunnittelu kuvaillaan yksityiskohtaisesti ja valmistetun koekytkentämallin suorituskyky varmistetaan laboratoriomittauksin. Tutkaetupään mitattu tehonkulutus on pienempi kuin 2.5 W. Ulostulon taajuusalue on 13.28 – 13.389 GHz ja ulostuloteho on noin 14 dBm. Vastaanottimen kohinaluku on 6.5 dB. Toteutetun tutkakorkeusmittarin suorituskyky todetaan hyväksi ja siinä on riittävästi jatkokehityspotentiaalia projektin seuraavaa vaihetta eli insinöörimallia varten.

---

**Avainsanat:** tutka, FMCW, korkeusmittari

---

## **Preface**

The research work for this licentiate thesis has been carried out in Harp Technologies Ltd. within European Space Agency's project "Assessment and Bread-boarding of a Planetary Altimeter (ABPA)". Many thanks to all the colleagues at Harp for fruitful conversations and efficient cooperation.

I would like to thank professor emeritus Antti Räisänen for supervising and helping one more student to finish his thesis. Unfortunately, professor Räisänen could not officially handle this to the end due to the bureaucracy. Therefore, thanks to professor Zachary Taylor for your contribution during finalizing the thesis.

I want to express my deepest gratitude to my wonderful wife and children. Without your support this thesis would still be a work in progress.

Vihti, August 26, 2019,

Teemu Ruokokoski

# Contents

<b>Abstract .....</b>	<b>2</b>
<b>Tiivistelmä.....</b>	<b>3</b>
<b>Preface .....</b>	<b>4</b>
<b>Contents.....</b>	<b>5</b>
<b>List of abbreviations.....</b>	<b>7</b>
<b>List of symbols .....</b>	<b>9</b>
<b>1. Introduction.....</b>	<b>11</b>
1.1 Background.....	11
1.2 Requirements .....	12
1.3 Contents of the thesis.....	13
<b>2. Planetary radar altimeters .....</b>	<b>14</b>
2.1 Radar applications .....	14
2.2 Reference altimeters with space heritage .....	15
2.2.1 HG8500 pulse radar .....	15
2.2.2 Terminal Descent Sensor.....	16
2.2.3 Huygens FMCW radar .....	17
2.3 Pulse and FMCW radar concepts .....	19
2.3.1 Basic principle of pulse radar .....	19
2.3.2 Basic principle of FMCW radar .....	21
2.4 Surface scattering model.....	24
2.5 Selection of operational frequency .....	26
2.6 Estimated range of the radar altimeter .....	27
<b>3. Design of the Ku-band FMCW radar .....</b>	<b>32</b>
3.1 Functional description .....	32
3.2 Design of functional components .....	33
3.2.1 Voltage controlled oscillator (VCO) .....	34
3.2.2 VCO controller .....	36
3.2.3 Power amplifier (PA) .....	37
3.2.4 Directional coupler and isolator .....	38
3.2.5 Low noise amplifier (LNA).....	43
3.2.6 Mixer .....	44
3.2.7 IF chain.....	49

3.3	Estimated power consumption and mass .....	50
3.4	Breadboard of the radar front-end .....	51
<b>4.</b>	<b>Measurements of functional components .....</b>	<b>53</b>
4.1	VCO measurements .....	53
4.2	VCO controller .....	55
4.3	S-parameters of RF components .....	55
4.3.1	LNA and PA .....	55
4.3.2	Directional coupler/isolator .....	56
4.3.3	Mixer .....	59
4.4	PA output power .....	60
4.5	Mixer conversion loss .....	60
4.6	IF chain measurements .....	61
4.6.1	IF filter .....	61
4.6.2	AGC amplifier .....	63
<b>5.</b>	<b>System level tests of the radar front-end .....</b>	<b>64</b>
5.1	Transmitter output power .....	64
5.2	Transmitter sweep bandwidth .....	65
5.3	Receiver noise figure .....	65
5.4	Power consumption, size and mass .....	67
5.5	Functionality tests of the radar front-end .....	67
<b>6.</b>	<b>Conclusions .....</b>	<b>74</b>
	<b>References .....</b>	<b>76</b>

## List of abbreviations

AGC	Automatic gain control
BJT	Bipolar junction transistor
CMOS	Complementary metal oxide semiconductor
COTS	Commercial of the shelf
CPU	Central processing unit
CW	Continuous wave
DC	Direct current
ECSS	European cooperation for space standardization
EEE	Electrical, electronic and electromechanical
EGSE	Electric ground support equipment
EM	Engineering Model
ESA	European Space Agency
FET	Field effect transistor
FM	Flight Model
FMCW	Frequency modulated continuous wave
GNC	Guidance, navigation and control
IF	Intermediate frequency
LIDAR	Light detection and ranging
LNA	Low noise amplifier
LO	Local oscillator
MMIC	Monolithic microwave integrated circuit
PA	Power amplifier
PCB	Printed circuit board
PRF	Pulse repetition frequency
PSU	Power supply unit
RF	Radio frequency
RFI	Radio frequency interference
RMS	Root mean square
RX	Receiver
SAW	Surface acoustic wave
SMT	Surface mount technology
SNR	Signal-to-noise ratio
SoW	Statement of work

TDS	Terminal descent sensor
TE	Transverse electric
TM	Transverse magnetic
TWG	Triangular wave generator
TX	Transmitter
VCO	Voltage controlled oscillator
VNA	Vector network analyzer



## List of symbols

$A$	area
$A_{eff}$	antenna effective area
$B$	bandwidth
$B_{IF}$	IF bandwidth
$B_n$	noise bandwidth
$c$	speed of light
$C$	surface roughness parameter in Hagfors' model in eq. (2.10 – 2.11); coupling in dB in eq. (3.1) and (3.6)
$D$	directivity in dB
$f$	frequency
$f_b$	beat frequency
$f_D$	Doppler frequency
$f_{IF}$	intermediate frequency
$f_{LO}$	local oscillator frequency
$f_m$	modulation frequency
$f_r$	pulse repetition frequency
$f_{RF}$	radio frequency
$F$	noise factor
$G$	gain
$G_0$	peak antenna gain
$h$	thickness of the substrate
$H$	altitude
$k$	Boltzmann's constant in eq. (2.24); coupling coefficient in eq. (3.4 – 3.6)
$l$	length of the directional coupler
$L$	loss
$N$	noise power
$NF$	noise figure
$P$	power
$P_{1dB}$	output power at 1 dB compression
$P_r$	received power
$P_t$	transmit power
$r$	radius
$R$	distance to the target

$R_H$	reflection coefficient for horizontal polarization
$R_V$	reflection coefficient for vertical polarization
$s$	spacing between the coupled lines
$S$	signal power
$S_{mn}$	scattering parameter
$S_{target}$	power density at target
$t$	time
$T$	temperature
$T_0$	room temperature 290 K
$T_a$	antenna temperature
$T_m$	modulation period
$T_r$	pulse repetition period
$T_{rec}$	receiver noise temperature
$T_{sys}$	system noise temperature
$th$	thickness of the substrate conductor
$v_r$	radial velocity
$V_{CC}$	supply voltage
$w$	width of the microstrip line
$Z_0$	characteristic impedance
$Z_{0e}$	characteristic impedance of the even mode
$Z_{0o}$	characteristic impedance of the odd mode
$\epsilon_r$	relative permittivity
$\lambda$	wavelength
$\lambda_g$	wavelength in the transmission medium
$\theta$	angle of incidence from vertical
$\theta_{3dB}$	half power beamwidth
$\theta_{rms}$	RMS surface slope
$\rho_0$	Fresnel power reflection coefficient for normal incidence
$\sigma$	radar cross section
$\sigma^0$	surface scattering coefficient
$\tau$	pulse width
$\tau_{sw}$	time delay of the TX/RX switch
$\varphi$	azimuth angle

# 1. Introduction

## 1.1 Background

Humans have been exploring beyond the Earth's atmosphere since 1957 when the first artificial satellite, Sputnik 1, was launched to a low Earth orbit. Soon after that, during the 1960's, we already started sending spacecrafts to other celestial bodies (e.g. the Moon, other planets, asteroids) for scientific missions.

A descent and landing system for a planetary exploration mission require a direct and reliable measurement of a planet lander's altitude. Some events (e.g. releasing the parachute, activation of retro rockets) in an entry, descend and landing sequence are triggered based on the information provided by the altimeter. There are basically two technological choices for measuring the ground distance of the planetary lander, i.e. radar and laser radar (or LIDAR = light detection and ranging). The working principle of both technologies is based on emitting electromagnetic waves towards the target. The transmitted signals reflect from the target and return to the receiver. The distance can then be calculated from the time it takes for the signal to travel to the target and back.

Altimeters based on both technologies have been successfully used in various exploration missions. Due to the much longer wavelength compared to light, microwave radar signals penetrate better through various media. Therefore, radar altimeters can measure through opaque atmosphere, clouds, dust storms etc. The shorter wavelength of the LIDAR altimeter signal leads to higher accuracy and resolution at short distances, but at the same time the radar altimeters have longer operating distance due to the lower attenuation of the transmitted signal. One main disadvantage of the radar technology compared to LIDAR is that the equipment dimensions (especially the antennas) are increased due to the longer wavelength. As the radar and LIDAR technologies differ from each other and excel in different operating conditions, they can be used as redundant systems in the same mission. The European Space Agency is aiming at smaller landers for the future exploration missions which impose excessive design constraints for mass, size and available power of the lander. Therefore, also the altimeter sensor of the planet lander must be minimized in terms of mass and power.

This thesis is based on the work done by Harp Technologies Ltd. within the European Space Agency's project "Assessment and Bread-boarding of a Planetary Altimeter (ABPA)". The project objective was to analyse, design and bread-board a hybrid planetary altimeter (i.e. radar and LIDAR) for ESA's exploration programme [1]. ESA has identified two mission scenarios which need the altimeter: the Mars network science mission and the High Precision Lander for Mars. Harp Technologies was responsible for the radar instrument and LusoSpace (Portugal) was responsible for the LIDAR instrument of the hybrid altimeter. The author served as Chief Design Engineer of the radar front-end module in this project. In addition to the radar front-end, antennas for the radar altimeter were also developed by Harp Technologies. The central processing unit (CPU) and power supply units (PSU) of the radar altimeter belong to the radar back-end and these are not included in this thesis. The prime contractor of the project was EFACEC Electric Mobility (Portugal) who was responsible for the detailed design of the radar back-end.

Author's contribution was the system level design of the radar front-end, developing the RF part of the radar front-end (excluding antennas and the IF part) and laboratory testing (including the whole radar front-end with antennas). The RF part of the radar consists of VCO, PA, directional coupler/isolator, LNA and mixer. M.Sc. Josu Uusitalo was responsible for the system level modelling and simulations of the radar (including surface scattering modelling) and the design of the antennas. Lic.Sc. (Tech) Kari Lehtinen was responsible for the detailed design of the IF part and electronics (i.e. AGC, IF filter and VCO controller) of the radar front-end.

## 1.2 Requirements

The requirements of the altimeter are given in the Statement of Work (SoW) document [1] for the project "Assessment and Bread-boarding of a Planetary Altimeter (ABPA)". Some of the requirements given in the SoW are fully applicable only for the final space hardware and the performance requirements for the breadboard model were somewhat reduced. For example, the mass and dimensions of the breadboard module were allowed to be larger than in the final Flight Model (FM). However, the breadboard was required to comply with the functional requirements and to have sufficient improvement potential for the later stages of the project. The main functional requirements for the altimeter are presented in Table 1.

Table 1. The functional requirements for the altimeter.

Parameter	Requirement	Notes
Operational envelope for altitude	3 km down to 10 m	The altitude range in which the altimeter shall supply data to the GNC loop for action.
Ambiguity envelope for altitude	7 km down to 3 km	The altitude range in which the altimeter shall supply data but the GNC loop is passive.
Maximum G-load	40 g	To survive Earth launch and the Mars entry and parachute deployment.
Maximum mass	Breadboard: 1.68 kg FM: 1 kg	Including electronics box and the required antennas. Consequently, the target mass for the radar front-end was set to 0.67 kg
Maximum dimensions	Breadboard: 15 x 13 x 10 cm <sup>3</sup> FM: 15 x 10 x 10 cm <sup>3</sup>	Consequently, the mechanical envelope target of 15 x 10 x 7 cm <sup>3</sup> was set for the radar front-end.
Maximum power consumption	5 W	5 W for the entire altimeter assembly. The target for the radar front-end was set to 2.5 W.

Design temperature	Operational (FM): -40 °C to 60 °C  Non-operational: -50 °C to 70 °C	Operational (breadboard): -20 °C to 60 °C
Minimum refresh rate	20 Hz	50 Hz optional
Altitude inaccuracy	0.33% H $\pm$ 0.8 m at maximum	i.e., 10.7 m at 3 km altitude and 0.8 m at 10 m altitude

### 1.3 Contents of the thesis

A radar front-end for a planetary altimeter is assessed, designed, bread-boarded and tested in this Licentiate thesis.

Chapter 2 introduces some previously developed planetary altimeters, a theoretical background for pulse and FMCW radars, a surface scattering model and selection of operational frequency. Also, a maximum measurement altitude of the FMCW radar is estimated in Chapter 2.

In Chapter 3, the design of a Ku-band FMCW radar front-end is described in detail.

A verification of the developed radar front-end is performed with laboratory tests and measurements. The testing of the individual components is presented in Chapter 4 and the measurements of the whole radar front-end are presented in Chapter 5.

The work is summarized and the results of this thesis are discussed in Chapter 6.

## 2. Planetary radar altimeters

### 2.1 Radar applications

The history of radar can be traced back to James Clerk Maxwell's work on electromagnetism. In 1865, Maxwell published his theory "A Dynamical Theory of the Electromagnetic Field", which implied that electromagnetic fields travelled through space as waves with the speed of light. Maxwell's mathematical theory was proved in 1887, when Heinrich Hertz discovered the existence of the electromagnetic waves with his series of experiments. This gave basis for many later inventions, such as television, radio and radar.

The first idea of radar came soon after, in 1904, when German engineer Christian Hülsmeyer patented and built a device to detect ships. The device was rather simple, because the device, "telemobiloscope", was only able to detect the presence of the ships, but not their accurate range [2].

The radar technology advanced significantly during the World War II, when different radar devices were developed independently in many countries, e.g. in the UK, USA, Germany, France, Soviet Union and Japan. The most important early military application was to notify and detect the range of approaching hostile aircrafts. Hence the word itself, radar, is an acronym for "Radio Detection and Ranging". By the end of the war, hundreds of different radar systems had been developed.

Since the early military applications, the use of radar technology has widened to numerous fields. The non-military applications include: air and terrestrial traffic control, vehicle anti-collision systems, autonomous vehicles, navigation, surveillance systems, meteorological monitoring, geological observations, altimetry etc. Due to the development in electronics and signal processing techniques, the use of radar applications has entered our everyday life. The development will not stop, the radar systems will become smaller and cheaper in the future, and as a result can be used in various new areas.

Obviously, radar systems have also been used in space exploration programs since the beginning. Radar altimetry is basically a technique for measuring height. The measurement also yields valuable other information that can be used in many applications. The first Earth observation satellites were launched during 1970s (Skylab, GEOS3 and Seasat) and since then, precise satellite altimetry missions have changed the way we view Earth. Currently, multiple satellites are mapping the surface of Earth and providing scientific information for various applications. Parameters that can be inferred from radar altimeter measurements include sea surface height, wind speeds, ocean topography, land and sea ice, geoid modeling etc. The information provided by satellites is the key asset for accurate weather forecasts and studying the climate change. The ESA publication "Radar altimetry tutorial" [3] gives thorough overview of past, current and future satellite altimetry missions and their applications.

This thesis focuses on one important radar altimeter application, i.e. landing safely on a planetary surface.

## 2.2 Reference altimeters with space heritage

Since the 1960s, several successful altimeter aided landings on the Moon, Mars, Venus and Titan have been performed. Considering only radar altimeters, both pulse and frequency modulated continuous wave (FMCW) radar concepts have been used in the planetary altimeters. The current activity has strict requirements for the power consumption, mass and measurement range. In order to initially estimate the performance of the pulse and FMCW radar technologies, the radar altimeters that have space heritage from the 1990s and 2000s were surveyed.

### 2.2.1 HG8500 pulse radar

Honeywell HG8500 pulse radar altimeter has been applied on successful Pathfinder and Mars Exploration Rovers (MER) missions. A photograph of the Honeywell HG8500 pulse radar is shown in Figure 1 and the main specifications are presented in Table 2.

The operational center frequency of the HG8500 radar is 4.3 GHz and the specified altitude range is 0 – 2500 m. The radar utilizes antennas with rather wide beamwidths ( $50^\circ$ ), and therefore an obvious solution to improve the maximum range would be to use higher gain antennas. The maximum unambiguous range can be estimated from the specified pulse repetition frequency (PRF = 25 kHz). The maximum unambiguous range for the HG8500 is approximately 6 km, and thus it fulfills the requirement (3 km) for the current application. However, the specified maximum power consumption (16 W) largely exceeds the current requirement of 2.5 W for the radar front-end. In order to fulfill the specified requirement, the transmit power of the radar must be reduced. Obviously, this would lead to the maximum range reduction at the same time.

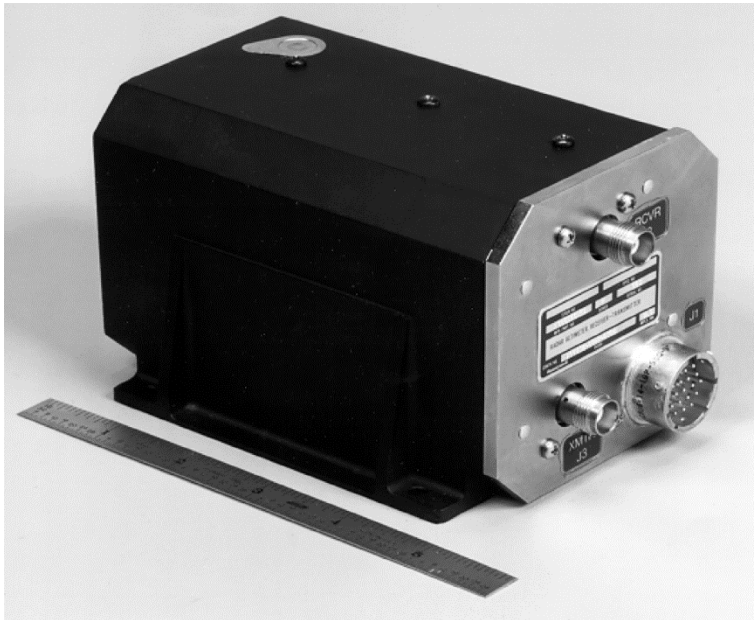


Figure 1. Honeywell HG8500 series pulse radar altimeter [4].

Table 2. Key parameters of Honeywell HG8500 pulse radar altimeter [1][4].

Parameter	Value
Altitude range	0 – 2500 m
Altitude accuracy	$\pm (0.9 \text{ m} + 3\%)$ analog $\pm (0.9 \text{ m} + 1\%)$ digital
Frequency	$4300 \pm 10 \text{ MHz}$
Power consumption	max. 16 W
Transmit power	5 W peak
Pulse length	30/225 ns
Pulse repetition frequency (PRF)	25 kHz
Size	86 mm x 86 mm x 142 mm
Mass	1.4 kg (including antennas)
Number of antennas	2
Antenna beamwidth	$50^\circ$
Antenna gain	9.5 dBi
Antenna size	89 mm x 89 mm

### 2.2.2 Terminal Descent Sensor

More recent example of the pulse radar is the Terminal Descent Sensor (TDS) developed for the Mars Science Laboratory mission. This planetary lander successfully delivered Curiosity rover on Mars, in the year 2012. A hardware illustration of the TDS is shown in Figure 2. Some data on the TDS has been published in the literature [5], and the main specifications are given in Table 3.

The TDS has the center frequency of 35.75 GHz and the altitude range of 10 – 3500 m. The radar contains six unique antennas for the accurate acquisition of velocity and altitude. The power consumption of the whole system is not given, but it largely exceeds the current requirement as the transmit power per antenna is 2 W.

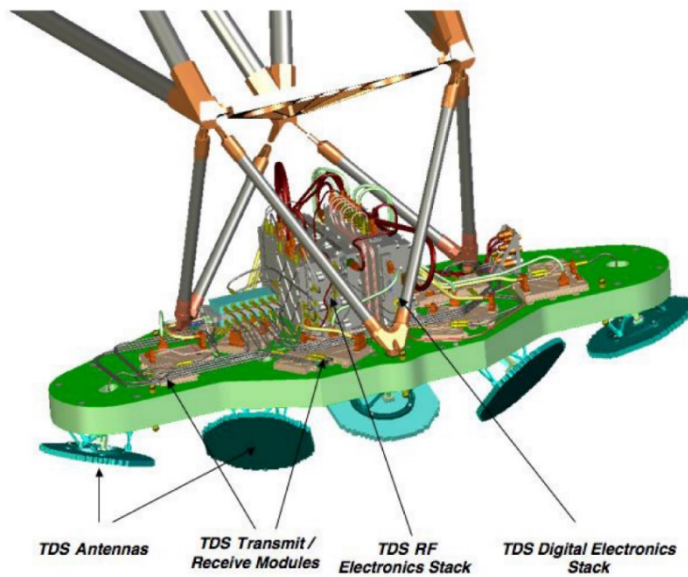


Figure 2. Hardware illustration of the TDS [5].



Table 3. Key parameters of the TDS pulse radar.

Parameter	Value
Altitude range	10 – 3500 m
Altitude accuracy	2%
Frequency	35.75 GHz
Transmit power	2 W peak (per antenna)
Range of pulse lengths	4 – 16000 ns
Range of pulse repetition intervals	75 – 250 $\mu$ s
Number of antennas	6
Antenna beamwidth	$< 3^\circ$

### 2.2.3 Huygens FMCW radar

FMCW radars have also a strong heritage in space missions. The Huygens radar altimeter developed by Ylinen Electronics, Finland, demonstrated reliable operation when landing on Saturn moon, Titan, in 2005. A photograph of the Huygens FMCW radar altimeter with the most of the microwave components visible is shown in Figure 3. As can be seen in the photograph, a level of integration is rather low. Especially, a voltage controlled oscillator (VCO) and filters consume a lot of space. Significant reduction of size and mass would be possible with modern microwave components.

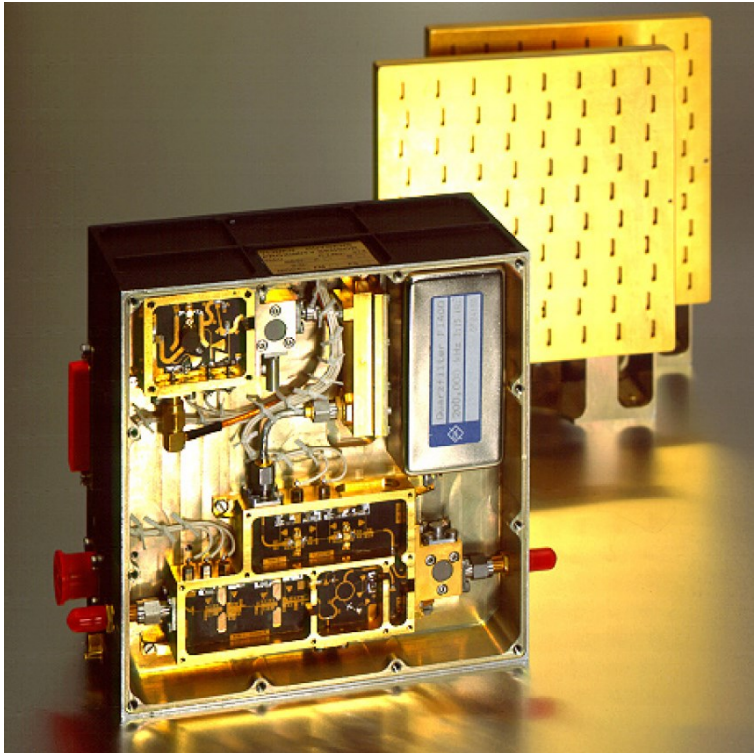


Figure 3. Huygens FMCW radar altimeter, showing antennas and opened microwave compartment [6].

The main specifications of the Huygens radar altimeter are presented in Table 4. The altimeter consisted of two redundant radars, operating at center frequencies 15.4 GHz and 15.8 GHz. The achieved altitude range was from 20 km down to 150 m. The radar applied a triangular wave modulation with transmitter sweep bandwidth 30 MHz. The ramp rate of the modulating signal was adjusted so that the constant beat frequency 200 kHz was obtained from the IF output.

The specified size and mass of the Huygens radar slightly exceed the requirements for the current activity, but as stated before, these can be reduced. Also, the maximum power consumption value 3.2 W is promising, and it is foreseen that the power consumption can be reduced by proper selection of active components. The Huygens radar operated down to the altitude of 150 m, and thus improvement is required to extend the range down to 10 m. Higher modulating frequencies are required at lower altitudes, while still maintaining the linearity of the modulating waveform. Further, the dynamic range requirement of the radar receiver changes with lower altitudes. It must be ensured that higher received power at low altitudes does not saturate the receiver.

Several possible improvements to the Huygens radar altimeter are discussed in [7]. Suggested enhancements include, e.g., improvement of modulation ramp linearity, acquisition of temperature data for temperature dependent components, minimizing the system noise temperature and acquisition of data from external systems to correct probe attitude related errors.

Table 4. Key parameters of Huygens FMCW radar altimeter [7].

Parameter	Value
Altitude range	150 m – 20 km
Altitude accuracy	uncalibrated: 10% calibrated: 2%
Frequency	15.4 GHz and 15.8 GHz (two redundant radars)
Transmitter sweep bandwidth	30 MHz
Intermediate frequency (IF)	200 kHz
IF bandwidth	15 kHz
Power consumption	max. 3.2 W
Transmit power	100 mW
Size	200 mm x 200 mm x 100 mm
Mass	2 kg (including antennas)
Number of antennas	2
Antenna beamwidth	8°
Antenna gain	26 dBi

## 2.3 Pulse and FMCW radar concepts

### 2.3.1 Basic principle of pulse radar

A simple method to extract a distance to a target surface is to transmit a train of RF energy pulses towards the target. A part of the signal is reflected back and received with the radar system. As the electromagnetic signal travels with the speed of light  $c$ , the range can be determined from the time delay  $\Delta t$  between the transmitted and received pulses. Assuming the received power is high enough to be detected, the target range  $R$  is simply

$$R = \frac{c\Delta t}{2}, \quad (2.1)$$

Figure 4 illustrates the basic operational principle of the pulse radar with ideal transmitted and received signals. The transmitted energy has the pulse width  $\tau$  and the next pulse is sent after the pulse repetition interval  $T_r$ . The pulse repetition frequency (PRF) is therefore  $f_r = 1/T_r$ . The attenuated echo is received after the time delay  $\Delta t$ .

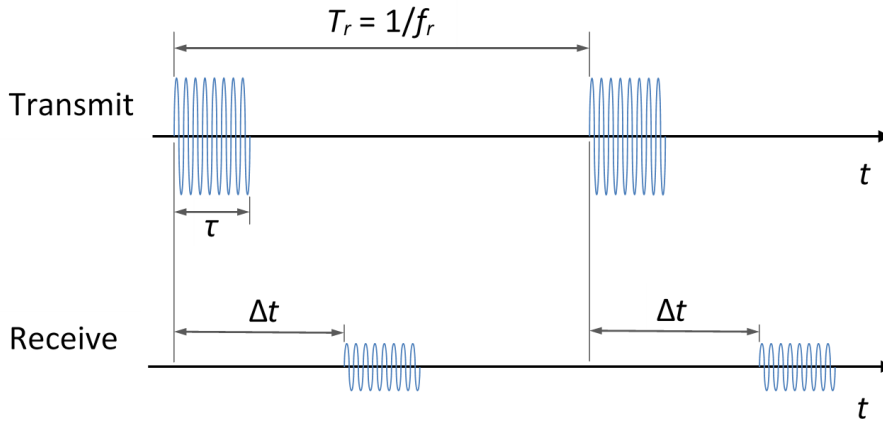


Figure 4. Transmitted and received pulses in the pulse radar.

A typical monostatic pulse radar utilizes one antenna, which is used for both transmit and receive. A transmit/receive switch is used to change the operation mode of the radar. Good isolation between the transmitter and receiver is achieved, because the transmitter waits quietly during the receive. However, this has the effect that the maximum and minimum unambiguous ranges are limited by the pulse repetition period and the pulse width, respectively.

First, the pulse echo must be received before the transmission of the next pulse begins. If the time delay exceeds the pulse repetition period (i.e.  $\Delta t > T_r$ ), the received echo is treated as it would be the echo of the next pulse, and as a result there will be an ambiguity in the range. Thus, the maximum unambiguous range is defined as [8]

$$R_{max} = \frac{cT_r}{2} = \frac{c}{2f_r} \quad (2.2)$$

Secondly, the pulse echo cannot be processed before the full pulse has been transmitted. The minimum range is therefore limited by the pulse width. In practice, the transmit/receive switch cannot change its state instantaneously, and the time delay of the switch,  $\tau_{sw}$ , must be included when defining the minimum unambiguous range. Thus, the minimum unambiguous range is

$$R_{min} = \frac{c(\tau + \tau_{sw})}{2} \quad (2.3)$$

Solving the PRF from equation (2.2) for the current planetary altimeter (the required maximum unambiguous range  $R_{max} = 3$  km) leads to the requirement  $f_r < 50$  kHz. Adopting the maximum value  $f_r = 50$  kHz is beneficial, because it maximizes the number of pulses received during the specified refresh period (i.e.  $1/(20 \text{ Hz}) = 50$  ms). The effective signal-to-noise ratio of the received echo can be improved by using pulse integration in the radar receiver. The specified maximum measurement altitude of the planetary altimeter is 7 km. The chosen  $f_r = 50$  kHz will lead to range ambiguities at altitudes above 3 km, but the lander is required to resolve this by the use of timing, acceleration or other supporting data. The main design challenge of the pulse radar altimeter is to achieve sufficient signal-to-noise ratio at high altitudes, given that the available transmit power is very limited. The total power consumption of the radar front-end is required to be less than 2.5 W, which leaves very small amount of power for the actual transmitted pulses.

Another design challenge for the pulse radar altimeter is established by the required minimum operational altitude,  $R_{min} = 10$  m. First assuming an ideal transmit/receive switch with  $\tau_{sw} = 0$ , and then solving equation (2.3) leads to the required pulse width  $\tau < 7$  ns at the range  $R_{min} = 10$  m. State-of-the-art PIN diode switches are able to achieve switching times  $\tau_{sw} < 10$  ns. Introducing realistic switching time to equation (2.3) leaves no room for the pulse width. Thus, the simple pulse radar concept based on one transmit/receive antenna is not applicable for this planetary altimeter, if the switching time is higher than approximately 2 ns. In that case, simultaneous transmission and receiving will be necessary, which creates constraints for the required transmitter/receiver isolation.

Very short pulses required at low altitudes introduce also a problem at high altitudes. Detectability of the signal depends on the received pulse energy and noise power [9]. Thus, to improve the signal-to-noise ratio (SNR) at high altitudes, the radar average transmitted power must be increased by increasing the pulse width. Therefore, the pulse radar for the current application would require adjustable pulse width.

Another method to improve the maximum range is to utilize pulse compression techniques. In the pulse compression technique, the frequency or phase of the transmitted pulse is swept (typically linearly) during the pulse. The bandwidth of the pulse increases compared to the bandwidth of unmodulated pulse of the same duration. A matched filter is used in the receiver to compress the pulse to a shorter length. Thus, the signal-to-noise ratio is improved. However, the pulse compression technique increases the radar design complexity compared to the ordinary pulse radar.

Using the pulse radar concept for the current planetary altimeter would create several design challenges due to the stringent performance requirements. Therefore, another solution is preferred.

### 2.3.2 Basic principle of FMCW radar

Unmodulated continuous wave (CW) radars utilize pure sinusoidal waveforms. They can be used to extract target radial velocity, because the center frequency of echoes from moving targets will be shifted by the Doppler frequency,  $f_D$ . The advantage of the CW radar is its simplicity as the Doppler frequency shift is determined by [9]

$$f_D = \frac{2v_r f_0}{c}, \quad (2.4)$$

where  $v_r$  is the radial velocity difference between the target and the radar and  $f_0$  is the transmitted frequency. The Doppler frequency shift is positive for approaching targets and negative for receding targets.

However, the CW radar is fundamentally incapable of determining the range of the target. In order to measure the range, the transmit waveform must be modulated. A common technique is to frequency modulate a microwave oscillator, which serves as both transmitter and local oscillator of the radar. These radars are called frequency modulated continuous wave (FMCW) radars. The modulating waveform may be a linear sawtooth, triangular, sinusoidal or some other form.

Using triangular modulation is convenient in the radar altimeters, because the Doppler shift caused by the moving target can be averaged out. The frequency-time relationships of the linear triangular wave modulation are shown in Figure 5. The red curve in Figure 5a is the transmitted frequency with rising and falling ramp. The received signal (shown in green color) has a similar form. However, the received signal is delayed by the signal propagation time,  $\Delta t$ , resulting in the difference or beat frequency  $f_b$  between the transmitted and received signals. If the target is approaching (which is the case for planetary landers), the received frequency is also shifted higher by the Doppler frequency  $f_D$ . The Doppler shift shown in the figure is largely exaggerated for representation purposes.

The beat frequency can be obtained by mixing the transmitted and received signals, and the result is shown in Figure 5b. During the rising ramp, the Doppler frequency produced by the approaching target decreases the resulting beat frequency, and during the falling ramp the Doppler frequency increases the beat frequency. Moreover, the Doppler frequency is somewhat higher when the transmitted signal is above its center frequency and lower when the transmitted signal is below its center frequency. However, the effect is so small that this lack of parallelism between the transmitted and received signals is not shown in Figure 5a. If target radial velocity does not change drastically, the Doppler shift can be cancelled by averaging the beat frequency over the modulation period  $T_m$ . The maximum anticipated velocity, and thus Doppler frequency, of the target must be taken into account when deciding the bandwidth for the IF filter. The IF bandwidth must be at least twice the Doppler frequency in order to keep the received beat frequency in the band during the modulation period.

It must also be noted that the beat frequency falls to zero, when the frequency ramp changes direction. These blanking periods must be considered when extracting the range from the beat frequency. It can be solved by signal processing and possibly discarding non-informative parts of the beat frequency.

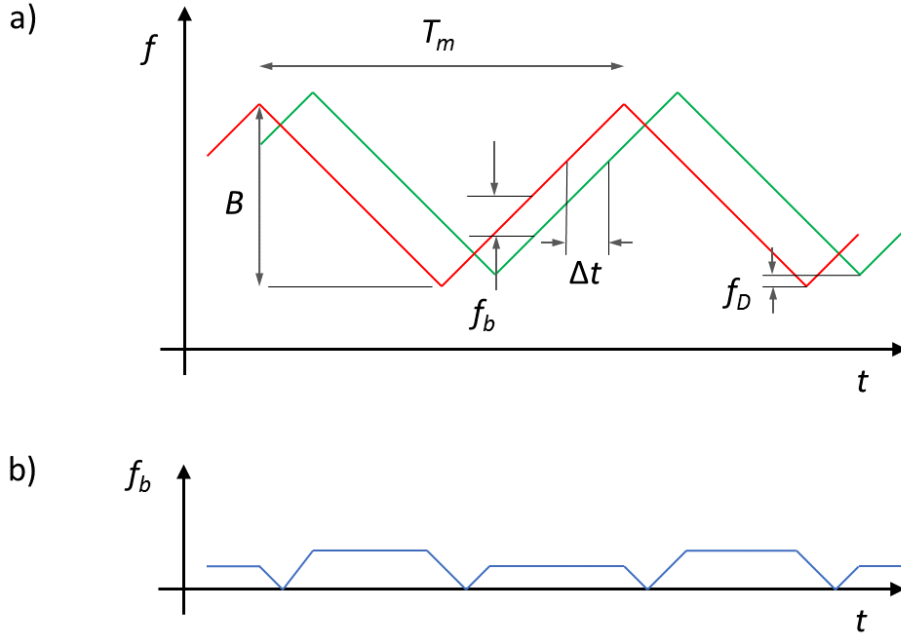


Figure 5. Frequency-time relationships in FMCW radar: a) transmitted signal (red curve) and received echo (green curve) for triangular modulation, and b) resulting beat frequency for triangular modulation.

The distance to the target may be determined by using a constant ramp rate and measuring the beat frequency. However, this is not convenient if the distance varies over several orders. In this planetary altimeter case, the required altitude range is from 7 km down to 10 m. Thus, the range of beat frequency variation would also be large, resulting in the requirement of wideband receiver filter and amplifiers.

The IF bandwidth can be reduced by using a variable ramp rate and keeping the beat frequency constant despite changing distance to the target. The beat frequency is related to the ramp rate  $df/dt$  and the signal propagation time  $\Delta t$  [10]:

$$f_b = \frac{df}{dt} \Delta t = \frac{df}{dt} \frac{2R}{c} \quad (2.5)$$

The ramp rate is related to the transmitter sweep bandwidth  $B$  and the modulation period  $T_m$ :

$$\frac{df}{dt} = \frac{2B}{T_m} \quad (2.6)$$

The modulation frequency  $f_m$  is the inverse of the modulation period  $T_m$ :

$$f_m = \frac{1}{T_m} = \frac{f_b}{2B\Delta t} \quad (2.7)$$

Now, using equations (2.5) – (2.7), the distance  $R$  to the target can be solved:

$$R = \frac{f_b c}{2 \frac{df}{dt}} = \frac{f_b c}{4f_m B} \quad (2.8)$$

The requirement for the relative range accuracy given in Table 1 is  $0.33\% \pm 0.8$  mm, which is 1-sigma accuracy. When solving the range  $R$  from equation (2.8), the accuracy of the whole range measurement depends on the accuracy of three parameters, i.e. the measured beat frequency  $f_b$ , the transmitter sweep bandwidth  $B$  and the modulation frequency  $f_m$ .

The frequency change in the transmitted radar signal is achieved by sweeping a tuning voltage of a voltage controlled oscillator (VCO) with certain modulation frequency. The modulation frequency  $f_m$  can be controlled very accurately by using a digital microcontroller. However, the VCO output frequencies are generated with analogue electronics which have a limited accuracy. Therefore, the resulting VCO output sweep bandwidth  $B$  has uncertainty  $\Delta B$ . It is also possible that the sweep bandwidth depends on the temperature. Consequently, as the sweep bandwidth cannot be controlled accurately, it must be characterized and the uncertainty have to be taken into account in the range calculation.

Another parameter which affects the range calculation is the measured beat frequency  $f_b$ . Ideally, the beat frequency is kept constant in the servo-type FMCW radar. In practice, the beat frequency has certain deviation,  $\Delta f_b$ , which has an influence on the range accuracy. There are many non-idealities which affect the beat frequency deviation. First, a sufficient signal-to-noise ratio (SNR) is required to extract the beat frequency from the noise. Poor signal-to-noise ratio affects the accuracy of the beat frequency especially at high altitudes. The second non-ideality is related to the target geometry. The target is a continuous ground surface, which causes randomly fluctuating echo in both amplitude and phase. The spectrum of the echo is wider than for the ideal point-like target, and therefore the range retrieval will get more inaccurate. Also, an error is introduced in the measured beat frequency, if the phase of the signal is not solely determined by the signal delay. Thus, the stability of the transmitted signal (sweep linearity and phase noise) also affect the accuracy of the beat frequency.

Thus, two main contributors to the calculated range error are the accuracy of the transmitter sweep bandwidth and the accuracy of the beat frequency. These error sources are not correlated, and thus the relative range accuracy can be expressed as:

$$\frac{\Delta R}{R} = \sqrt{\left(\frac{\Delta B}{B}\right)^2 + \left(\frac{\Delta f_b}{f_b}\right)^2} \quad (2.9)$$

The required relative range accuracy  $\Delta R/R$  is 0.33%. The design goals for the radar can be established by allocating the total requirement equally between the two contributors (i.e. 0.23% for both).

The main design concern in FMCW radars is transmitter/receiver isolation. Because the transmitter is operating constantly, the direct leakage to the receiver can obscure weak target echoes. The problem is usually tackled by using separate antennas for the transmitter and receiver. If the geometry permits, the antennas can be widely separated to achieve good isolation.

The FMCW radar concept is technically simpler than the pulse radar. Given that the available transmit power is limited, the anticipated maximum measurement distance is also greater due to the continuous transmission.

## 2.4 Surface scattering model

A radar backscattering from a surface can be estimated with a variety of methods. One method to describe the terrain scattering is Hagfors' model [11]. The Hagfors model assumes a Gaussian distribution of surface heights, where the surface is described by the surface roughness parameter  $C$  and the Fresnel normal reflection coefficient  $\rho_0$ . The assumptions for the surface-slope distributions and correlation functions in the Hagfors model have been criticized, but the model is still widely used in planetary applications. The Hagfors model usually shows good agreement with near-nadir radar measurements of planetary objects. In this model the surface scattering coefficient  $\sigma^0$  with different angles of incidence  $\theta$  has the form [12]

$$\sigma^0(\theta) = \frac{C\rho_0}{2}(\cos^4\theta + C\sin^2\theta)^{-3/2} \quad (2.10)$$

The surface roughness parameter  $C$  in the model is accepted to be related to the root-mean-square (RMS) of the surface slope distribution  $\theta_{rms}$  [13]

$$C = \tan^{-2}\theta_{rms} \quad (2.11)$$

Any arbitrary electromagnetic wave can be divided into horizontal and vertical polarization components. Horizontal polarization is also called TE-polarization as the electric field of the incident wave is perpendicular to the normal vector. In vertical polarization or TM-polarization, the magnetic field component is perpendicular to the normal vector. Assuming a non-magnetic surface material, Fresnel amplitude reflection coefficients for horizontal and vertical polarizations are [14]



$$R_H = \frac{\cos \theta - \sqrt{\varepsilon_r - \sin^2 \theta}}{\cos \theta + \sqrt{\varepsilon_r - \sin^2 \theta}} \quad (2.12)$$

$$R_V = \frac{\varepsilon_r \cos \theta - \sqrt{\varepsilon_r - \sin^2 \theta}}{\varepsilon_r \cos \theta + \sqrt{\varepsilon_r - \sin^2 \theta}} \quad (2.13)$$

The power reflection coefficient for the normal angle of incidence (i.e.  $\theta = 0^\circ$ )  $\rho_0$  can now be retrieved from

$$\rho_0 = \left| \frac{1 - \sqrt{\varepsilon_r}}{1 + \sqrt{\varepsilon_r}} \right|^2, \quad (2.14)$$

where  $\varepsilon_r$  is the relative permittivity of the surface material.

In order to estimate the scattering coefficient  $\sigma^0$  for the surface of Mars, estimates for the relative permittivity  $\varepsilon_r$  and the RMS surface slope  $\theta_{rms}$  are required. Some measurement data on  $\varepsilon_r$  and  $\theta_{rms}$  for Mars have been published [14] [15]. According to [14], bistatic radar experiments were conducted during years 1977-78 by the Viking orbiter spacecraft. The results for Hellas Basin and the equatorial region showed the RMS surface slope to be  $\theta_{rms} = 4 - 5^\circ$ . The estimates for the relative permittivity ranged from  $\varepsilon_r = 1.5$  in certain parts of the north polar region to  $\varepsilon_r = 4.0$  in Syrtis Major. Syrtis Major is also the smoothest region in Mars, where areas with  $\theta_{rms} < 0.25^\circ$  have been detected. Additionally, [14] reports that generally for Mars, plains are smoothest ( $\theta_{rms} < 2^\circ$ ) and sand dunes are roughest ( $3.5 < \theta_{rms} < 7^\circ$ ).

More recent measurements of the surface roughness were performed by the Mars Global Surveyor spacecraft. According to [15], the RMS slopes show an average of  $\theta_{rms} = 3 - 10^\circ$  in the southern highlands and  $\theta_{rms} = 0.2 - 0.8^\circ$  in the northern lowlands.

Based on the above reference data, the surface scattering coefficient  $\sigma^0$  for Mars can be estimated with equation (2.10). Three landing scenarios for poorly, typical and highly reflective surfaces are shown in Figure 6. The poorly reflective surface with  $\varepsilon_r = 1.5$  and  $\theta_{rms} = 10^\circ$  is the scenario, where the landing occurs at the highlands. It is questionable if the relative permittivity of the surface has the lowest value occurring at the same time with steep slopes, because the low permittivity usually requires that the surface material is not dense. Therefore, this poorly reflective situation is considered as the worst case scenario. The best case scenario is landing to Syrtis Major, which is flat and has the highest reported relative permittivity. The highly reflective case in the graph is calculated with values  $\varepsilon_r = 4.0$  and  $\theta_{rms} = 0.5^\circ$ . The third graph for the scattering coefficient is the scenario, where the surface parameters are considered to be close to typical ( $\varepsilon_r = 3.0$  and  $\theta_{rms} = 5^\circ$ ). This typical case is used as a reference, when estimating the return power with the radar equation. When the incident angle of the antenna beam is close to vertical, the surface scattering coefficient is approximately  $\sigma^0 = 6$  dB in the typical case. The attitude of the lander (and thus the incident angle of the antenna beam) is assumed to remain in the range  $0 - 10^\circ$  during the operation

of the altimeter. The effects of the surface parameters and the incident angle on the received power can be estimated from the calculated graphs when testing the developed radar front-end.

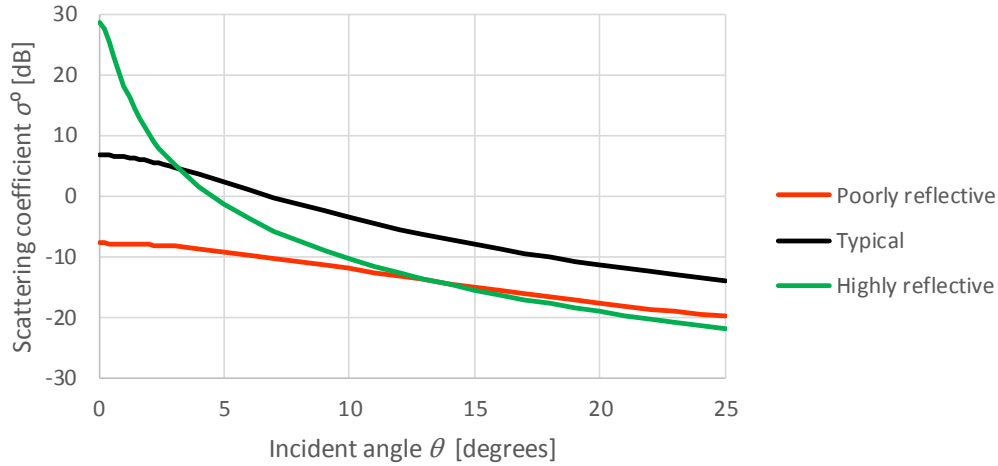


Figure 6. Mars surface scattering coefficient based on Hagfors' model, assuming poorly reflective surface (red line:  $\epsilon_r = 1.5$ ,  $\theta_{rms} = 10^\circ$ ); typical surface (black line:  $\epsilon_r = 3.0$ ,  $\theta_{rms} = 5^\circ$ ); and highly reflective surface (green line:  $\epsilon_r = 4.0$ ,  $\theta_{rms} = 0.5^\circ$ ).

## 2.5 Selection of operational frequency

Previous planetary landers have been utilizing mostly C- (i.e. 4 – 8 GHz) or Ku-bands (i.e. 12 – 18 GHz) for the operating frequency [1]. However, size and mass of microwave components decrease with increasing frequency. Especially, the antenna size needed to achieve a desired antenna beamwidth has an impact on the frequency selection. Therefore, also Ka-band (i.e. 26.5 – 40 GHz) was considered for the radar front-end.

Contrarily, the availability of the space qualified microwave components is much better for the C- and Ku-bands than for the Ka-band. After surveying European manufacturers, it became evident that the choice of components for the Ka-band is so limited that it is not economically feasible to choose this frequency band for the current activity. However, it is foreseen that the availability of the microwave components will improve in the future, and then the Ka-band will become a viable option for the operating frequency.

International frequency allocations are not valid in other planets. However, it is deemed necessary to test the developed radar front-end with balloon flights on Earth. Therefore, an authorized frequency band must be selected. In the C-band, the frequency range 4.2 – 4.4 GHz is allocated for radar altimeters, and in the Ku-band the available choices are 13.25 – 13.4 GHz and 15.35 – 15.4 GHz [16]. The latter frequency range in the Ku-band is foreseen as too narrow (only 50 MHz) for the sweep bandwidth of the radar front-end, and thus rejected.

The frequency band 4.2 – 4.4 GHz is widely used in aircraft radar altimeters. This frequency band results in reasonably sized antennas, and the frequency is low enough that the attenuation of rain does not limit the range of the radar. On Mars, the attenuation of atmospheric gases is negligible. The attenuation due to water vapour and oxygen is estimated to be less than 0.01 dB/10 km at 32 GHz, and even smaller at lower frequencies [17]. However, the attenuation due to

relatively common dust storms has to be considered. According to [17], the attenuation  $L_{dust} = 3$  dB is the worst case estimate for 32 GHz signals over the 10 km dust cloud. The attenuation at lower frequencies is achieved by scaling with  $1/\lambda$ . Scaling to 4.3 GHz and 13.3 GHz leads to the worst case attenuations  $L_{dust} = 0.04$  dB/km and  $L_{dust} = 0.12$  dB/km, respectively. The attenuation of the severe dust storm is so low for both frequency choices that a definite conclusion for the selection cannot be drawn.

Separate antennas for the transmit and receive are required for the FMCW radar. The exact diameter of the planetary lander is not yet known in the breadboarding phase of the project, but the diameter is estimated to be approximately 60 cm. Based on the preliminary analysis for the maximum measurement altitude and the accuracy of the altimeter, the half-power beamwidth  $\theta_{3dB}$  of the antennas must be less than  $10^\circ$  to fulfill the specifications. The diameter of the antennas can initially be estimated from  $\theta_{3dB} \simeq \lambda/d$  [18]. Thus, at 4.3 GHz the antenna diameter is  $d = 40$  cm and at 13.3 GHz the antenna diameter is  $d = 13$  cm, if the half-power beamwidth is  $10^\circ$ . It can be concluded that the frequency 4.3 GHz leads to too large antenna size in this application. The choice of the operational center frequency is therefore 13.3 GHz.

## 2.6 Estimated range of the radar altimeter

The received power  $P_r$  is required for the calculation of the signal-to-noise ratio and estimated maximum range of the radar. If the transmitted power is  $P_t$  and the gain of the transmit antenna is  $G$ , the power density at the target distance  $R$  is obtained from [19]

$$S_{target} = \frac{P_t G}{4\pi R^2} \quad (2.15)$$

The surface of the target reradiates the intercepted electromagnetic energy in all directions. The radar cross section  $\sigma$  of the target is defined as the ratio of the reflected power in the direction of the radar to the incident power density. The radar cross section depends on many parameters, such as transmitted frequency, target geometry, orientation and material. The power received by the radar is then

$$P_r = \frac{P_t G}{4\pi R^2} \frac{\sigma}{4\pi R^2} A_{eff}, \quad (2.16)$$

where  $A_{eff}$  is the effective area of the receiving antenna. The effective aperture of the antenna is related to its gain by

$$A_{eff} = \frac{\lambda^2}{4\pi} G \quad (2.17)$$

Inserting equation (2.17) to (2.16) leads to the simplest form of the radar equation for monostatic radars:

$$P_r = \frac{P_t G^2 \lambda^2 \sigma}{(4\pi)^3 R^4} \quad (2.18)$$

Equation (2.18) is not accurate enough for predicting the range in practical situations. This overly simplified radar equation neglects various losses (such as atmospheric attenuation and system losses). Moreover, the target cross section and the minimum detectable signals are statistical in nature, and the received signals are corrupted with noise.

Radar altimeters transmit signals towards the ground surface. The ground surface is a distributed target and the backscattered signal is caused by various scatterers within the area illuminated by the radar. The target radar cross section is given by

$$\sigma = \sigma^0 A, \quad (2.19)$$

where  $\sigma^0$  is the backscattering coefficient (or the normalized reflectivity per unit area) and  $A$  is the illuminated surface area.

The received power can be expressed as a surface integral over the illuminated area. Thus, the area-extensive form of the radar equation is [20]

$$P_r = \frac{P_t \lambda^2}{(4\pi)^3} \int_A \frac{G^2 \sigma^0}{R^4} dA \quad (2.20)$$

Equation (2.20) assumes a uniformly illuminated target area. However, the antenna radiation pattern is not uniform in practice, and therefore the antenna beam must be approximated when the actual shape is not yet known. A Gaussian, circularly symmetric antenna pattern is assumed for the initial range estimation. The function for the Gaussian antenna pattern is [21]

$$G(\theta) = G_0 e^{-2.773 \frac{\theta^2}{\theta_{3dB}^2}}, \quad (2.21)$$

where  $G_0$  is the peak antenna gain and  $\theta_{3dB}$  is the half-power beamwidth.

The geometry associated with equation (2.20) is shown in Figure 7. The surface area element  $dA$  inside the illuminated area can be expressed in spherical coordinates:

$$dA = R \sin \theta \frac{R}{\cos \theta} d\theta d\varphi = R^2 \tan \theta d\theta d\varphi \quad (2.22)$$

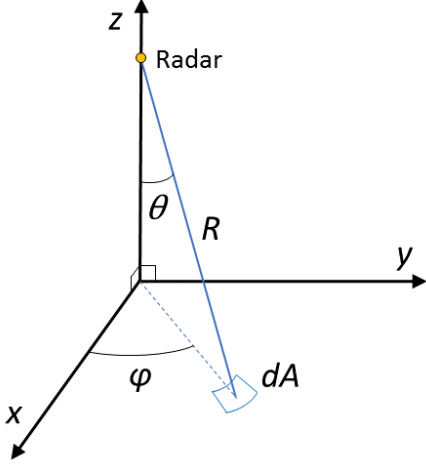


Figure 7. The geometry of the radar equation for the distributed target (after [9]).

Although the FMCW radar uses separate antennas for transmit and receive, the planetary altimeter is quasi-monostatic as the antennas are close to each other and are based on the same design. Therefore, assuming Gaussian antenna patterns and the Hagfors model for the surface scattering coefficient, the received power  $P_r$  can be calculated using a numerical integration from

$$P_r = \frac{P_t \lambda^2}{(4\pi)^3} \int_0^{2\pi} \int_0^{\pi/2} \frac{G^2(\theta) \sigma^0(\theta) \tan \theta}{R^2} d\theta d\varphi \quad (2.23)$$

The maximum measurement altitude can be estimated by evaluating the signal-to-noise ratio (SNR) as a function of range. The signal-to-noise ratio is defined by [9]

$$SNR = \frac{P_r}{P_n} = \frac{P_r}{k T_{sys} B_n}, \quad (2.24)$$

where  $P_n$  is the noise power,  $k$  is the Boltzmann constant,  $T_{sys}$  is the system noise temperature and  $B_n$  is the noise bandwidth. The noise bandwidth of the receiver is approximately the same as the IF bandwidth (i.e.  $B_{IF} = 30$  kHz). The system noise temperature for the cascaded receiving system with a cable between the antenna and the receiver, is given by

$$T_{sys} = T_a + T_{cable}(L_{cable} - 1) + L_{cable} T_{rec}, \quad (2.25)$$

where  $T_a$  is the antenna temperature,  $T_{cable}$  is the physical temperature of the cable,  $L_{cable}$  is the cable loss and  $T_{rec}$  is the effective receiver noise temperature.

The receiver noise temperature  $T_{rec}$  can be solved from the receiver noise factor  $F$

$$T_{rec} = T_0(F - 1), \quad (2.26)$$

where  $T_0$  is 290 K.

The antenna temperature  $T_a$  depends on the antenna pattern, frequency and antenna efficiency in a rather complicated way. For the initial range estimates, it is often assumed that  $T_a = T_0$ .

System parameters applied to predict the range of the FMCW radar altimeter are summarized in Table 5.

Table 5. Initial system parameters to analyse the range of the FMCW radar.

	Symbol	Value
<b>Transmitter</b>		
Center frequency	$f$	13.3 GHz
Center wavelength	$\lambda$	0.0225 m
Transmit power	$P_t$	13 dBm
<b>Antenna</b>		
Peak gain	$G_0$	24 dB
Beamwidth	$\theta_{3dB}$	10°
Antenna temperature	$T_a$	290 K
Antenna cable loss	$L_{cable}$	0.8 dB
Cable temperature	$T_{cable}$	290 K
<b>Receiver</b>		
Noise bandwidth	$B_n$	30 kHz
Receiver noise figure	$NF$	6 dB (i.e. $F = 3.98$ )
Receiver noise temperature	$T_{rec}$	864.5 K
System noise temperature	$T_{sys}$	1388 K
<b>Ground surface</b>		
Poorly reflective surface	$\epsilon_r$	1.5
	$\theta_{rms}$	10°
Typical surface	$\epsilon_r$	3.0
	$\theta_{rms}$	5°

The received power as a function of altitude was calculated by inserting Hagfors' model equation (2.10) and approximated Gaussian antenna pattern equation (2.21) into equation (2.23). The surface integral in equation (2.23) was solved using a numerical integration method (Simpson's rule). The signal-to-noise ratio was then calculated from equation (2.24). Attenuation due to atmospheric gases were not included in the calculations, because these are negligible on Mars. Also, the attenuation in the case of severe dust storm was omitted. As depicted in Section 2.5, the losses in the dust storm can be  $L = 0.12$  dB/km. At 7 km altitude, this leads to 1.7 dB degradation of the SNR compared to the calculated values.

Figure 8 shows the estimated SNR as a function of altitude for two cases: a poorly reflective ground surface and a typical surface. The received power and noise are both statistical quantities,

and therefore the SNR for reliable detection depends on the required probability of detection. It is here assumed that the required SNR is higher than 10 dB. Thus, in the case of typical backscattering conditions, the estimated maximum measurement altitude is approximately 50 km. The maximum measurement altitude drops to approximately 11.5 km with the poorly reflective surface. It can be concluded that there is enough reserve to fulfill the maximum altitude requirement (7 km) with the selected system parameters. The parameters shown in Table 5 are therefore used as target values for the design.

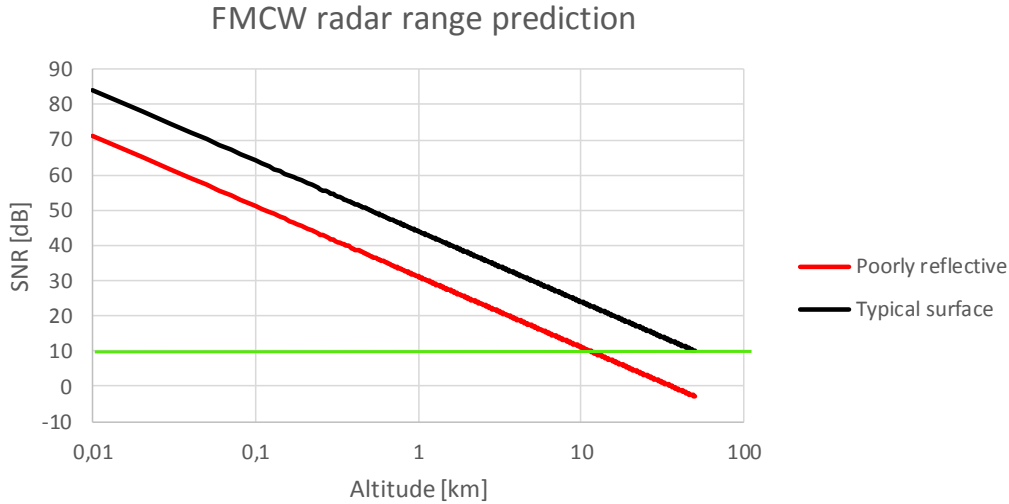


Figure 8. The signal-to-noise ratio (SNR) of the FMCW radar as a function of altitude, assuming poorly reflective surface (red line:  $\epsilon_r = 1.5$ ,  $\theta_{rms} = 10^\circ$ ) and typical surface (black line:  $\epsilon_r = 3.0$ ,  $\theta_{rms} = 5^\circ$ ). The green horizontal line shows the minimum SNR required for detection (SNR = 10 dB).

The dynamic input power range that the radar receiver should adapt to is a function of the minimum and maximum measurement altitudes (10 m and 7 km, respectively). The received power  $P_r$  was calculated at these altitudes, assuming poorly reflective and highly reflective backscattering conditions. The calculated results are shown in Table 6. The predicted input power range is from -30 dBm to -108 dBm. Thus, the target value for the dynamic range is 80 dB. The gain control of the radar receiver must adapt to this large dynamic range.

Table 6. The received power  $P_r$  at the minimum and maximum measurement altitudes (with transmit power  $P_t = 13$  dBm and normal beam incidence).

Surface	Altitude [m]	Received power [dBm]
Poorly reflective ( $\epsilon_r = 1.5$ , $\theta_{rms} = 10^\circ$ )	10	-51
	7000	-108
Highly reflective ( $\epsilon_r = 4.0$ , $\theta_{rms} = 0.5^\circ$ )	10	-30
	7000	-87

### 3. Design of the Ku-band FMCW radar

#### 3.1 Functional description

In the trade-off between pulse and frequency modulated continuous wave (FMCW) radar concepts, a servo type variant of the FMCW radar was evaluated to be the most suitable for the planet lander. In the selected FMCW technique, the carrier is modulated using a low frequency triangular waveform. The servo control constantly modifies the ramp rate of the modulating waveform so that the difference frequency (or the beat frequency)  $f_b$  remains constant despite the changing distance  $R$  to the target. This method is useful when the radar has only one primary target to measure, such as the ground surface in the planetary altimeter application. The main benefit of the servo control is that the IF bandwidth can be made narrow, which reduces the noise in the receiver and thus improves the signal-to-noise ratio.

The block diagram of the designed FMCW radar is shown in Figure 9. RF components are shown in green colour and IF components and antennas are shown in red colour in the block diagram.

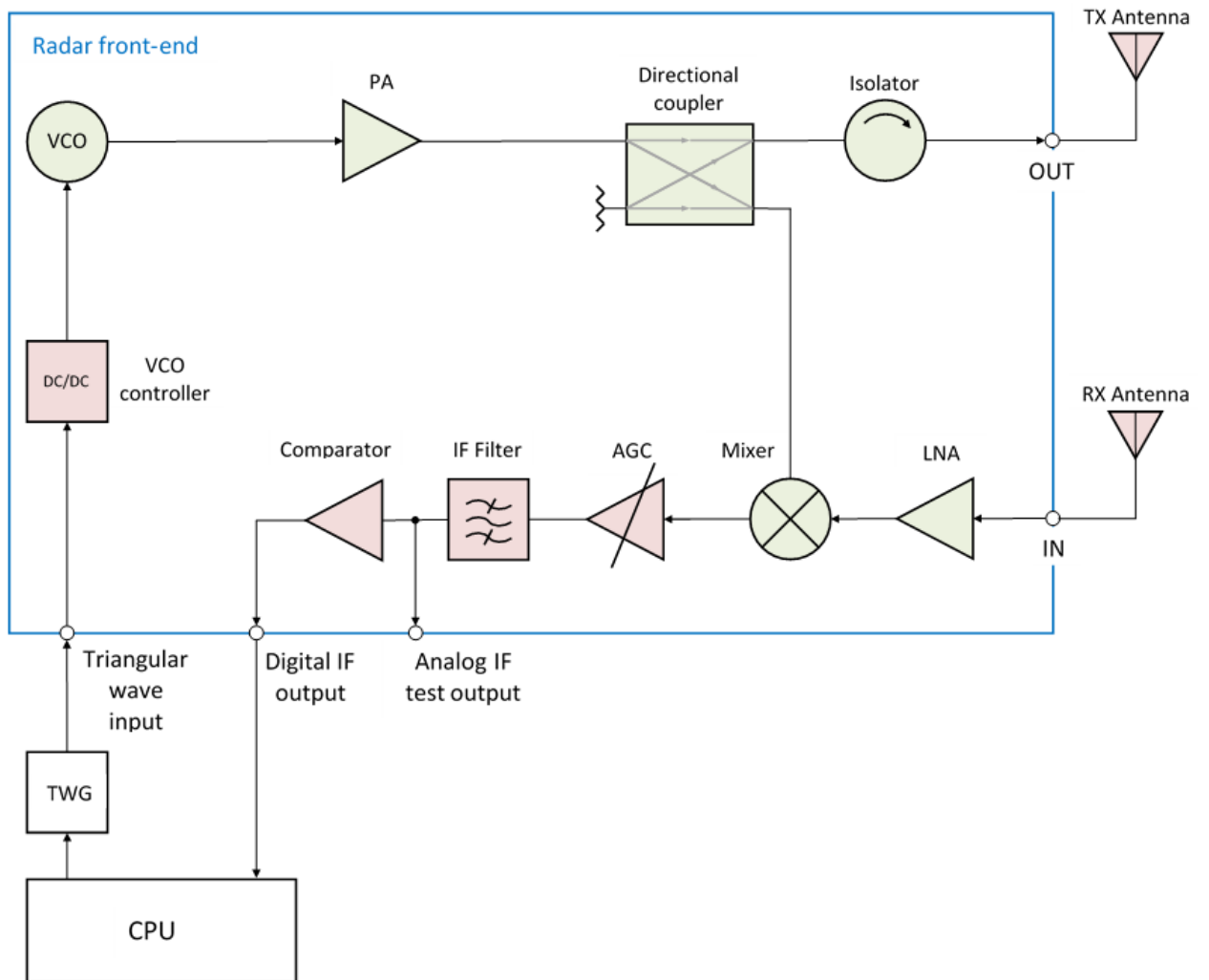


Figure 9. The block diagram of the FMCW radar altimeter (green: RF components, red: VCO controller, IF components and antennas).



In this radar design, the control of the frequency modulation is performed in the radar back-end processor (CPU) by measuring the beat frequency and adjusting the ramp rate accordingly. The carrier signal 13.3 GHz is generated in a voltage controlled oscillator (VCO) and it is modulated with a varying voltage at the input of the VCO. This modulating triangular wave is generated in the radar back-end. An additional level shifter (i.e. VCO controller) is needed at the input of the VCO to convert the voltage of the triangular wave to the correct level. The output frequency of the VCO is directly proportional to the input control voltage and the required modulation span for the frequency is 100 MHz (13.25 – 13.35 GHz) in this application. It is important to produce a clean, linear ramp over the whole sweep bandwidth, because the nonlinearity of the sweep would degrade the range resolution. The modulated signal is amplified to a desired level with a power amplifier (PA), before it is transmitted with a planar antenna array. An isolator is placed in the front of the antenna to suppress reflections coming back from the transmit antenna. The altimeter uses separate antennas for transmitting (TX) and receiving (RX).

A part of the transmit signal is taken to a receiver mixer by using a directional coupler. This signal is mixed with a returning ground echo and as a result, the beat frequency is obtained. The beat frequency is the difference between the transmitted and received signals at a given moment. In this servo-type radar the beat frequency is kept constant at 175 kHz by controlling the ramp rate of the modulating triangular wave. The returning ground echo is amplified with a low noise amplifier (LNA) before it is directed to a mixer.

The output of the receiver mixer (i.e. the beat frequency) is amplified with an active gain control (AGC) amplifier. The altimeter is required to operate over a wide range of distances from 7 km down to 10 m. When the returning ground echo is weak, the AGC will have high gain and when the signal is strong at low altitudes, the AGC will have low gain. A too-high signal level would saturate the receiver back-end and the AGC ensures that the signal is kept at the desired level. After the AGC, the beat frequency is filtered using an IF bandpass filter with 30 kHz bandwidth. Before sending the beat frequency to the back-end processor, the signal is converted to a square wave with a comparator. The distance can then be calculated from the period of the modulating triangular wave which was needed to establish the beat frequency 175 kHz.

### **3.2 Design of functional components**

The breadboard of the radar front-end is constructed from individual RF components with separate mechanical housings and from one electronics printed circuit board (PCB). This approach allows each component to be tested and tuned individually during the development. Once the performance of each individual component is satisfactory, the complete radar front-end module is assembled from the components. In the Engineering Model phase all the RF functions can be integrated into the same housing, which will result in significant mass and size reduction of the radar front-end module. Integrating the RF components into the single housing will also improve the performance, because attenuations related to cables and SMA connectors are excluded.

The housings of the RF components are manufactured from aluminum alloy with chromate conversion coating. The dimensions of the housings depend on the size of the designed PCB for each component. A substrate used for the RF components is Rogers RT/duroid 6002 [22]. The dielectric constant of the substrate is  $\epsilon_r = 2.94$ , the thickness of the substrate is  $h = 0.254$  mm and

the copper thickness is  $th = 17 \mu\text{m}$ . The conductors are plated with gold. This microwave substrate has low loss and excellent high frequency performance. The substrate is also space qualified and qualified PCB manufacturing lines for the substrate exist in Europe. The substrate of the electronics PCB is FR4 ( $\epsilon_r = 4.7$ ,  $h = 1.5 \text{ mm}$  and  $th = 17 \mu\text{m}$ ) and the PCB has 6 layers.

The RF housings are connected together using semi-rigid coaxial cables and straight-plug adapters. Voltages are connected through the housings using feedthrough capacitors. The housings are then attached on aluminum plates using bolts to form a rigid structure for the radar front-end module.

The requirement for the power consumption (max. 2.5 W for the radar front-end) imposed some compromises on the design. For example, an integrated downconverter could not be used because of its too-high power consumption. Instead, a passive balanced mixer based on Schottky diodes was designed. Also, a compromise had to be done regarding the output power of the radar when designing the power amplifier and choosing the component for it.

### 3.2.1 Voltage controlled oscillator (VCO)

The carrier frequency is generated in the VCO and it is frequency modulated using varying triangular waveform at the tuning input of the VCO. The VCO is based on Hittite HMC529LP5, which is a monolithic microwave integrated circuit (MMIC) VCO for 12.4 – 13.4 GHz with excellent phase noise performance [23]. A typical output power of the HMC529 is from +4 dBm to +10 dBm. The European Space Agency usually prefers European vendors for the chosen components, but an exception was done regarding the VCO. It is a known challenge that the availability of the space qualified European VCOs is very scarce. Also, the availability of suitable European microwave transistors to design the VCO from lumped elements is almost non-existent. Therefore, Hittite HMC529 was selected. During the breadboarding phase of the project, cost-effective commercial-of-the-shelf (COTS) components could be used while for the actual space mission, this component can be subjected to a mission level space qualification. The HMC529 component has linear frequency vs. tuning voltage response across the required sweep bandwidth 100 MHz, which was considered an important factor for the accuracy of the altimeter.

A microstrip technology was used in the design of the surrounding RF circuit. The HMC529 component was mounted on the Rogers RT/duroid 6002 substrate ( $h = 0.254 \text{ mm}$  and  $th = 17 \mu\text{m}$ ). Two bypass capacitors (100 pF and 2.2  $\mu\text{F}$ ) are required in the voltage supply pin of the HMC529. Non-qualified equivalents of the capacitors were used in the breadboard. The supply voltage ( $V_{CC} = +5 \text{ V}$ ) is connected through the mechanical housing using a feedthrough capacitor (Tusonix, FT 1000pF). The feedthrough capacitor is also a non-qualified equivalent of a component which has to be used in the Engineering and Flight Models of the radar.

The RF output pin and the tuning voltage pin of the component is connected to the 50  $\Omega$  microstrip line. The width of the 50  $\Omega$  microstrip line is  $w = 0.63 \text{ mm}$  for the RT/duroid 6002 substrate. The RF out/2 and RF out/4 pins of the HMC529 component are not used and the pins are left open in the design. The schematics of the designed VCO is shown in Figure 10.

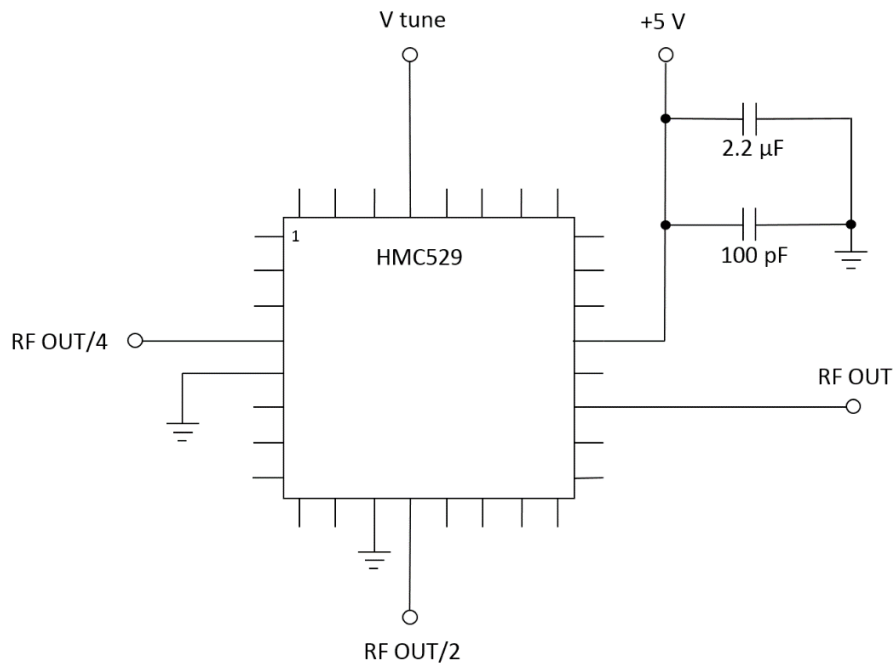


Figure 10. The schematics of the voltage controlled oscillator (VCO).

A mechanical component housing (size: 20.4 x 26.4 x 19 mm<sup>3</sup>) with 3.5 mm SMA wall mount socket was designed for the VCO. An absorber material DD-11393 from ARC Technologies Inc. was installed to the lid to suppress possible cavity resonances. The PCB was glued to the bottom of the housing using electrically conductive glue.

The output frequency of the VCO is somewhat temperature dependent. Thus, a temperature transducer (Analog Devices AD590M) was glued on the PCB, so that the temperature of the VCO can be monitored by the back-end processor. When the temperature is known, the effect on the output frequency can be compensated by changing the range of the tuning voltage. The manufactured VCO without the lid is shown in Figure 11.



Figure 11. The manufactured VCO.

### 3.2.2 VCO controller

The triangular wave to modulate the VCO is generated in the radar back-end. The modulating waveform has a voltage swing from -1.5 V to +1.5 V. Figure 12 shows the output frequency of the HMC529 component according to the tuning voltage [23]. The voltage swing to generate the required RF output frequency 13.25 – 13.35 GHz is approximately 8.5 – 9.5 V. Thus, the purpose of the VCO controller is to shift the level of the modulating triangular wave to the correct range. The VCO components also have batch-to-batch variations and therefore the final tuning voltage range will be adjusted after measuring the manufactured VCO.

The recommended operation range of the HMC529 component is 12.4 – 13.4 GHz. The operational sweep bandwidth 13.25 – 13.35 GHz of the radar altimeter is at the most linear region of the VCO component. The non-linearity of the sweep introduces additional variance to the measured beat frequency. If the range accuracy degrades too much due to the sweep non-linearity, an additional linearizer circuit would be needed in the VCO tuning voltage. However, it was predicted that the linearizer circuit will not be required and it was left as an option.

The central processing unit (CPU) in the radar back-end needs to know the actual sweep bandwidth to calculate the range accurately. If the sweep bandwidth increases or decreases from 100 MHz due to temperature, it degrades also the range accuracy, if the change is not taken into account. However, temperature compensation was not required in the breadboard model. It will be added in the Engineering Model, where also the sweep bandwidth will be characterized precisely.

Physically, the VCO controller is integrated on the electronics PCB together with the AGC amplifier, the IF filter and the voltage regulators. The voltage level shifter can be realized with an operational amplifier circuit, but the details of the design are not given here because the author was not responsible for the design of the electronics.

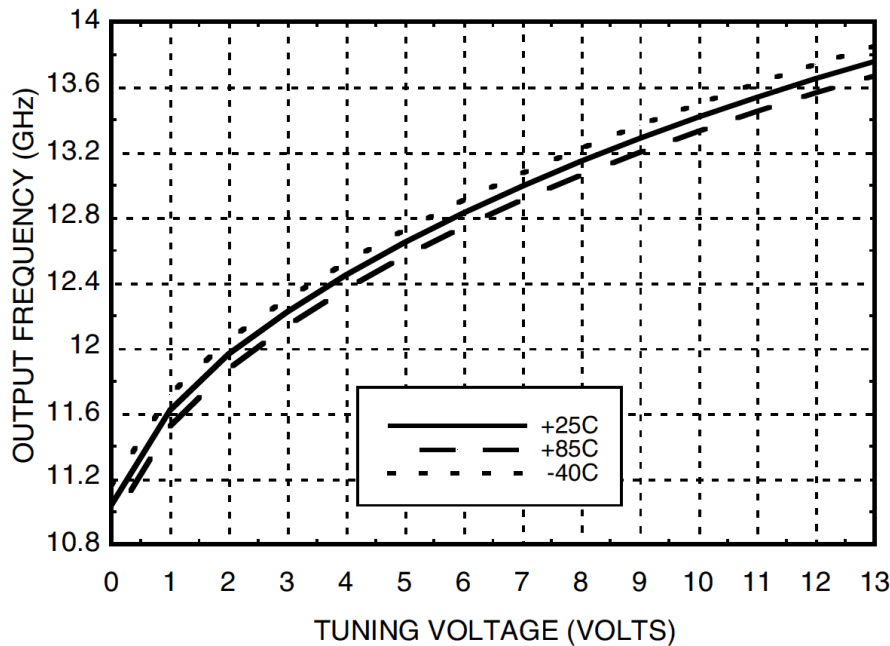


Figure 12. The VCO output frequency vs. tuning voltage [23].

### 3.2.3 Power amplifier (PA)

System level simulations of the radar front-end revealed that the required output power of the radar module should be approximately 12 – 14 dBm to achieve reliable measurements at 7 km even when the measurement conditions are poor. The design goal for the PA output power was set to 16 dBm as there are some losses in the directional coupler and the isolator before transmitting the signal with the antenna. The strict power consumption requirement for the radar front-end inflicted a choice of components. In terms of reliability, it would be beneficial to have some reserve in the output power of the radar, but the power consumption limit 2.5 W caused that the chosen component for the PA had to be a compromise between the output power and the power consumption.

The chosen component for the PA is CHA3666 from United Monolithic Semiconductor (UMS) [24]. It is a self-biased MMIC low noise amplifier for 5.7 – 17 GHz. Both commercial and space qualified versions of the component are available from UMS. CHA3666 has 20 dB gain at 13.3 GHz and 16 dBm output power at 1 dB compression. It has also low DC power consumption, 320 mW. Although CHA3666 is usually used as a low noise amplifier in receivers, it has high enough output power ( $P_{1dB} = 16$  dBm) to be used as the PA in this planetary altimeter application.

The CHA3666 component was mounted on the RT/duroid 6002 substrate. Designing the PCB is straightforward, because CHA3666 has internal matching circuits. The component only needs two bypass capacitors (100 pF and 10 nF) in the voltage supply. The RF input and output ports are connected to the 50  $\Omega$  microstrip lines ( $w = 0.63$  mm). The schematics of the PA is shown in Figure 13.

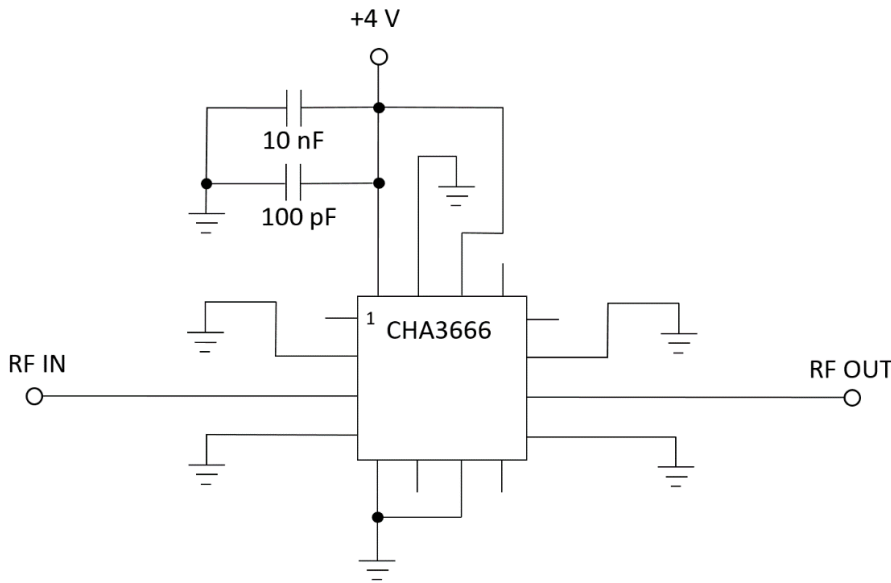


Figure 13. The schematics of the power amplifier.

The dimensions of the PCB were designed so that the same mechanical housing as for the VCO could be used. The absorber material (DD-11393) was glued to the lid of the enclosure and the temperature transducer (AD590M) was glued on the PCB to monitor the temperature of the PA. The supply voltage ( $V_{CC} = +4$  V) and the terminals of the transducer were directed through the housing using feedthrough capacitors (Tusonix FT 1000 pF). The RF input and output ports of the

mechanical housing have 3.5 mm SMA connectors. A photograph of the manufactured power amplifier is shown in Figure 14.

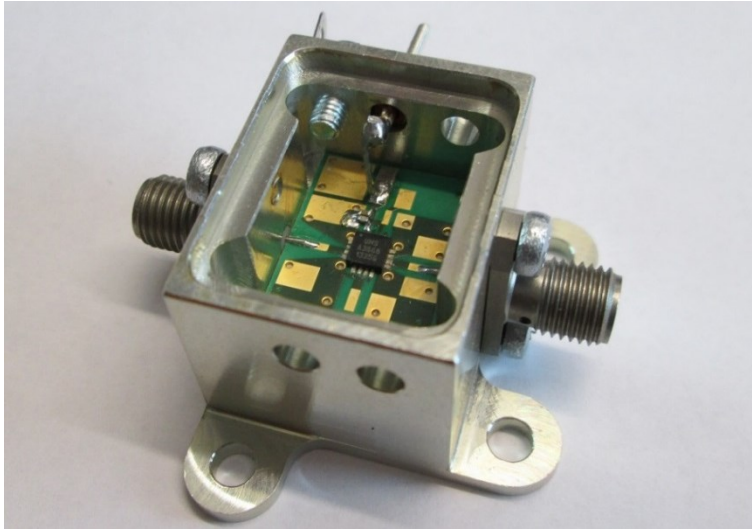


Figure 14. The manufactured power amplifier.

### 3.2.4 Directional coupler and isolator

A part of the transmit signal is taken to a local oscillator (LO) port of a receiver mixer using a directional coupler. The LO signal is mixed with the returning ground echo to produce the beat frequency. The requirement for the low power consumption inflicts the design so that a passive mixer is preferred in the radar. In order to turn on the diodes of the balanced mixer, the LO power of the signal must be in the range of 0 – 5 dBm. Otherwise the conversion loss of the mixer increases too much and will affect the noise figure of the receiver. The LO power can also be increased by using a buffer amplifier in the LO chain, but this was not an option in the radar altimeter design, because the amplifier would increase the power consumption.

As described in the earlier section, the output power of the PA will be approximately 16 dBm. This translates into 11 – 16 dB coupling requirement for the directional coupler. The requirement can be fulfilled with single section coupled microstrip lines.

A directional coupler is a 4-port device, which can be characterized by its coupling and directivity [25]:

$$C[dB] = 10\log \frac{P_1}{P_3} \quad (3.1)$$

$$D[dB] = 10\log \frac{P_3}{P_4} \quad (3.2)$$

When the power is fed to port 1, a part of the signal is coupled to port 3. Port 4 is isolated in the ideal case where all the ports are matched, but in practice some of the power leaks to port 4. The isolation of the directional coupler is defined as:

$$\text{Isolation}[dB] = 10\log \frac{P_1}{P_4} \quad (3.3)$$

An electromagnetic wave can propagate in coupled microstrip lines by two modes: even and odd mode. The even and odd modes have their own characteristic impedances, defined below:

$$Z_{0e} = Z_0 \sqrt{\frac{1+k}{1-k}} \quad (3.4)$$

$$Z_{0o} = Z_0 \sqrt{\frac{1-k}{1+k}} \quad (3.5)$$

The coupling coefficient  $k$  in equations (3.4) and (3.5) is related to the coupling  $C$  as

$$k = 10^{-C/20} \quad (3.6)$$

The highest value for coupling is achieved, when the physical length  $l$  of the coupled section is one quarter of the wavelength in the transmission medium:

$$l = \frac{\lambda_g}{4} \quad (3.7)$$

The dielectric medium is not homogenous in the coupled microstrip lines, and a part of the electromagnetic field extends to the air above the substrate. As a result, propagation velocities of the even and odd modes are different and this deteriorates the directivity of the simple coupled microstrip lines. The directivity of the coupler can be improved for example by using a wiggly line (sawtooth shape of coupled lines) structure. The wiggly lines equalize phase velocities of the even and odd mode signals and increase the directivity of the directional coupler [26]. The structure of the directional coupler utilizing the wiggly lines is shown in Figure 15. Design parameters for the structure are a length of the coupled section  $l$ , a gap between the coupled lines  $s$ , an average width of the coupled line  $w_c$  and a width of a single sawtooth  $d_w$ .

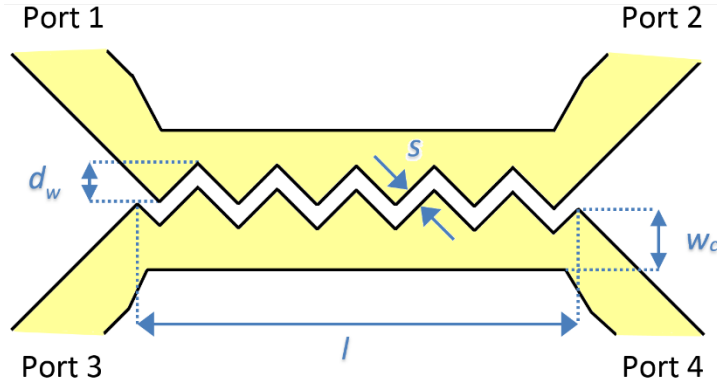


Figure 15. The wiggly line coupler with the design parameters.

The equations described above can be used as a starting point for the design. There are many graphs published in the literature (e.g. in [25]) how the even and odd mode characteristic impedances are related to the dimensions of the coupled microstrip lines. By using electromagnetic simulation tools, the design can be optimized in terms of insertion loss, coupling and isolation.

A planar microstrip structure using the RT/duroid 6002 substrate ( $h = 0.254$  mm,  $th = 17$   $\mu$ m) was designed and simulated with CST Microwave Studio. The coupling section is approximately quarter-wave long at the center frequency 13.3 GHz. In practice, a gap between the coupled lines determines the coupling if the other dimensions are optimized. The ECSS standard ECSS-Q-ST-70 “Design rules for printed circuit boards” [27] defines the minimum allowable spacing between the PCB tracks to be  $s = 120$   $\mu$ m. This gap width was used in the design to achieve the highest possible coupling. Other design parameters such as the length and the width of the coupled lines were optimized for the operating frequency of 13.3 GHz with CST Microwave Studio. The optimized parameters of the design are:  $w_c = 0.6$  mm,  $l = 3.8$  mm,  $s = 0.12$  mm and  $d_w = 0.35$  mm. The angles of the sawtooth sections are  $45^\circ$  with respect to the coupled lines. The coupled lines are tapered to the  $50\ \Omega$  microstrip lines ( $w = 0.63$  mm) of the ports. The tapered section is 1 mm long.

The simulated coupling of the directional coupler is shown in Figure 16. The coupling to port 3, which is the LO port of the mixer, is approximately 10.7 dB at 13.3 GHz. The manufacturing tolerances of the spacing between the coupled lines will affect the performance. As the gap is very narrow, the manufactured PCB will usually have wider gap than was specified. Also, sharp corners of the wiggly lines are difficult to realize and as a result the corners will be rounded after an etching process. These factors will worsen the coupling, but as long as the manufactured directional coupler has  $< 16$  dB coupling, the sufficient power level for the LO port of the mixer is ensured. This will be verified when measuring the manufactured directional coupler and the mixer.



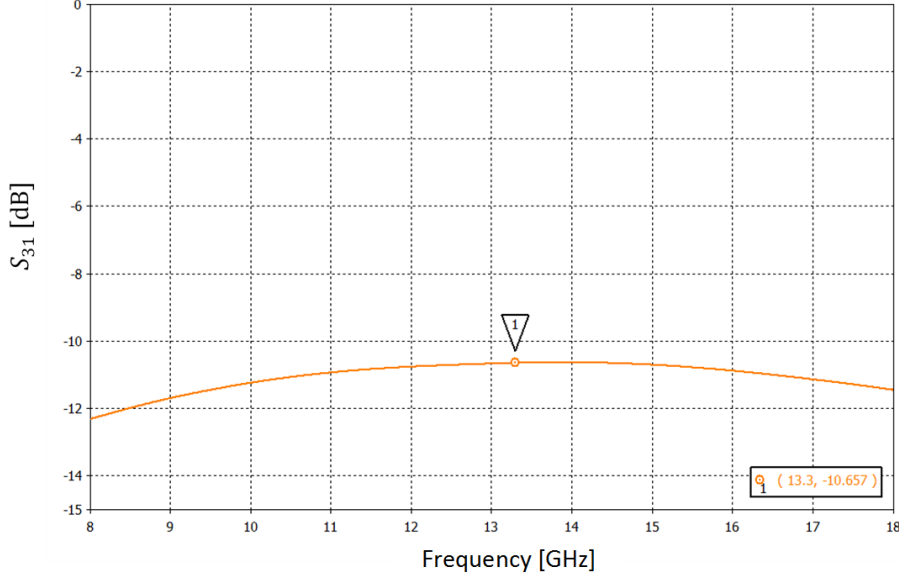


Figure 16. The simulated  $S_{31}$  (coupling) of the directional coupler.

The simulated insertion loss of the directional coupler is shown in Figure 17. Losses in the coupler will decrease the output power of the radar front-end module and therefore the insertion loss must be as low as possible. The insertion loss is approximately 0.7 dB at the center frequency 13.3 GHz.

Another parameter which can affect the performance of the radar front-end module is the isolation of the directional coupler. A part of the transmit signal will be reflected from the TX antenna depending on the matching of the antenna. The reflected signal can leak to the receiver mixer through the coupler. An isolator will be placed in the front of the TX antenna, but the isolation of the directional coupler will further suppress the leakage signal and ensure the proper operation of the receiver mixer. Figure 18 shows the simulated  $S_{41}$  of the directional coupler. Because the structure of the coupler is reciprocal, this is also the isolation between the antenna port and the LO port of the mixer. The isolation is approximately 23 dB at 13.3 GHz.

The final manufactured directional coupler has 50  $\Omega$  termination at port 4. The termination was realized on the PCB with a 50  $\Omega$  thin-film resistor and a radial stub. The radial stub has 30° angle and a radius  $r = \lambda_g/4$ . The termination can somewhat affect the performance of the directional coupler compared to the simulations done with ideal port 4. However, the termination was excluded from the simulations, because the exact model of the resistor was not available.

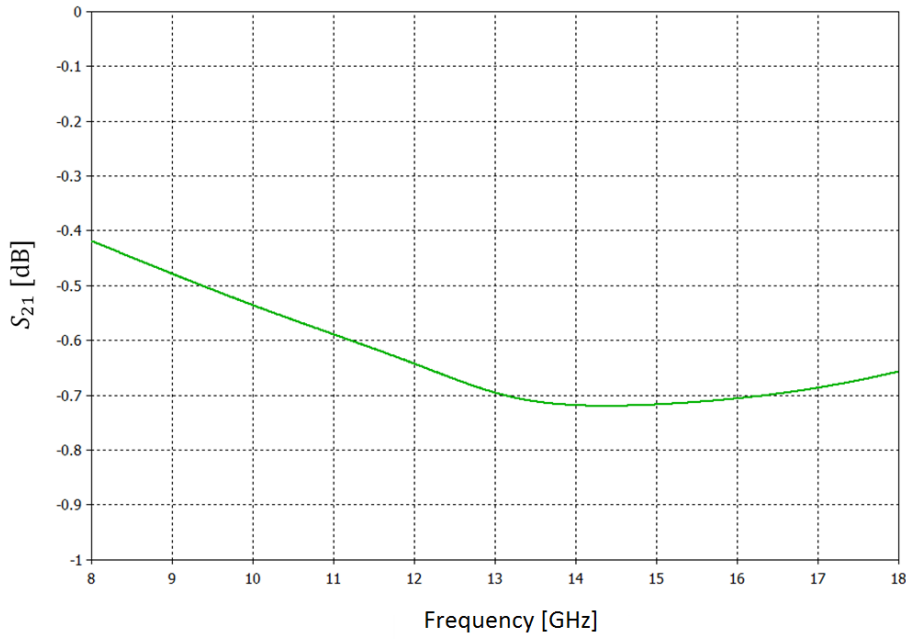


Figure 17. The simulated  $S_{21}$  (insertion loss) of the directional coupler.

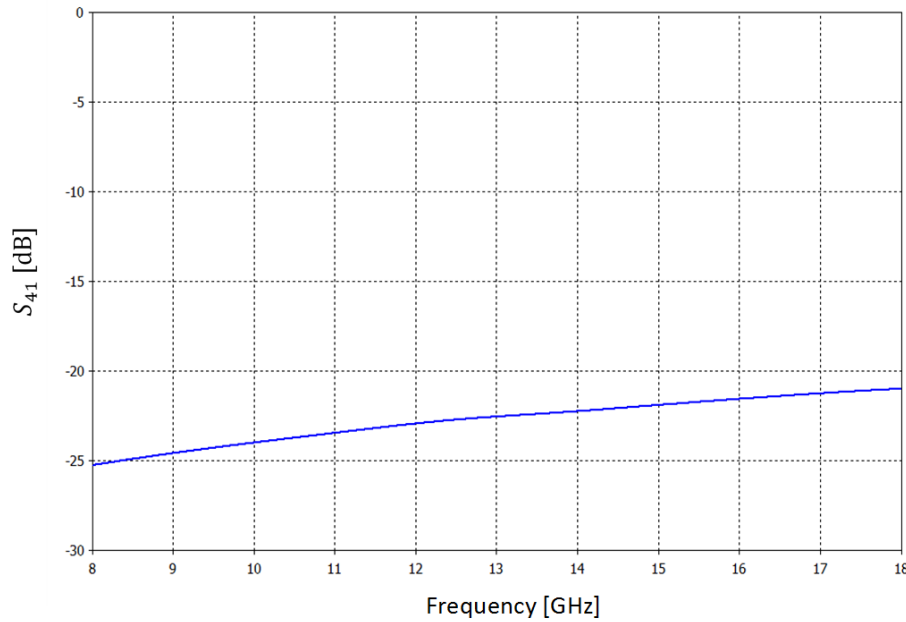


Figure 18. The simulated  $S_{41}$  (isolation) of the directional coupler.

An isolator is placed between the directional coupler and the TX antenna to prevent reflections from the antenna. The leakage to the receiver would increase the noise level of the radar and could also cause oscillations in the radar module. A drop-in type isolator NJ1140-07 from Cobham Microwave [28] is integrated within the same enclosure as the directional coupler. A typical isolation for the component is 20 dB and the insertion loss is 0.8 dB. The space qualified version for the isolator is also available. The drop-in isolator requires a milled insert in the mechanical housing (size: 34.4 x 26.4 x 19 mm<sup>3</sup>) where it is attached with two screws. The isolator is also glued on the housing with the electrically conductive glue to ensure good grounding of the component. The input and output terminals of the isolator are soldered to the 50  $\Omega$  microstrip lines.

Three ports (the RF input, RF output and coupled port) of the directional coupler and isolator have 3.5 mm SMA connectors. A photograph of the manufactured component is shown in Figure 19. The RF input is on the left, the RF output on the right and the coupled port to the mixer is on the top of the photograph.

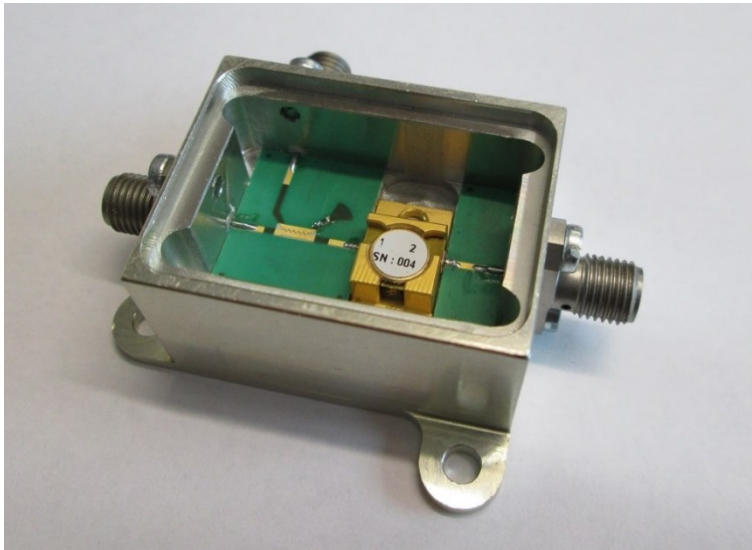


Figure 19. The manufactured directional coupler and isolator.

### 3.2.5 Low noise amplifier (LNA)

A low noise amplifier (LNA) at the input of the receiver amplifies the received ground echo. If the gain of the LNA is sufficiently high, the overall noise figure of the receiver is dominated by the LNA. Thus, it is necessary for the LNA to boost the received signal while adding as little noise as possible.

The LNA is based on the same MMIC component as the PA, CHA3666 from UMS. The same design for the PCB and the mechanical housing is used for the LNA as was used for the PA. CHA3666 has 20 dB gain and noise figure  $NF = 2$  dB at 13.3 GHz.

The radar uses two separate antennas for transmitting and receiving. The two antennas designed by M.Sc. Josu Uusitalo are identical in design and construction. The design is a patch antenna array with an 8 x 8 configuration of patches and the dimensions of the antenna structure are 148 x 148 x 4 mm<sup>3</sup>. It is initially assumed that the diameter of the lander is approximately 60 cm. If the antennas are situated at the opposite edges of the lander, the empty space between the antennas will be approximately 30 cm. It is also assumed that the housing of the lander is made of well conducting metal forming effectively a ground for the antennas. The simulated transmit-receive isolation (performed using CST Microwave Studio) with this construction is in the order of 60 dB. The output power of the radar front-end module will be approximately 14 dBm. This leads to the estimated leakage power of -46 dBm at the input of the receiver. As the LNA will saturate with the input power of approximately -5 dBm, the direct leakage of the transmit signal to the receive antenna will not saturate the LNA. There is also 40 dB margin if the leakage would be higher than anticipated. Accurate simulations of the transmit-receive isolation can only be performed after the final lander construction is known and added to the simulation model.

### 3.2.6 Mixer

A mixer is a device which is used to perform a frequency conversion of an input signal. The frequency conversion is achieved by using a non-linear element in the mixer circuit. In radar receivers, the input signal is usually downconverted to a lower frequency, where it is easier to execute further processing of the signal. The mixer has three ports: radio frequency (RF) port, local oscillator (LO) port and intermediate frequency (IF) port. When the mixer is used to downconvert the signal, the RF- and LO-ports are the input ports and the sum and difference of these frequencies are produced in the output IF-port. The output is then low-pass filtered to obtain only the difference frequency in the output.

When two excitation frequencies are fed to a strongly non-linear electronic component (such as Schottky-barrier diode or FET) multiple new frequency components are generated. The generated frequencies occur at a linear combination of the two excitation frequencies, which is shown in the equation below [29]:

$$f_{m,n} = mf_1 + nf_2 \quad (3.8)$$

In the microwave mixers, the LO signal is relatively large compared to the RF excitation. The harmonics of the RF signal are negligibly small and only its fundamental frequency is significant. Thus, the resulting frequencies in the mixer output are

$$f = f_{RF} + nf_{LO} \quad (3.9)$$

In the downconverters, the mixing frequency closest to DC is the IF output frequency, i.e.

$$f_{IF} = |f_{RF} - f_{LO}| \quad (3.10)$$

The other mixing products are usually harmful and must be suppressed with filters or using a proper choice for the mixer structure.

The mixer can be realized using a single non-linear electronic component but usually a single-balanced (two non-linear elements) or a double-balanced (four non-linear elements) structure is preferred to obtain better overall performance. For example, better isolation between the ports and rejection of spurious responses and intermodulation products can be achieved with the balanced structures [30]. The main disadvantage of the balanced mixer is that the required LO power is larger than in the single-element mixer because the LO power is divided into two or four elements.

The mixer circuits can further be divided into passive and active mixers. In the passive mixers the power level of the output signal is lower than the power level of the input signal, i.e., the mixer has conversion loss. The active mixers use an amplifying element to increase the power of the output signal and thus have conversion gain. The choice of the mixer type largely depends on the application.

In the FMCW radar, the frequency of the received ground echo differs from the transmitted signal. The ground echo is directed to the RF-port of the mixer and a part of the transmit signal is directed to the LO-port. The difference frequency is obtained in the IF-port. In the servo-type FMCW radar where the period of the modulating signal is constantly adjusted, the difference frequency is also called the beat frequency. In this planetary altimeter application, the passive single-balanced structure was chosen for the mixer mainly because of tight power consumption requirements. In the single-balanced mixer, two diodes are connected by using a  $90^\circ$  or  $180^\circ$  hybrid.

The  $180^\circ$  hybrids are more common in the microwave applications, because they have some benefits over the  $90^\circ$  hybrids. The  $180^\circ$  hybrids have usually larger bandwidth, better spurious and intermodulation rejection and the RF and LO ports are easier to match [31]. A popular design when utilizing the microstrip technology is a ring or rat-race hybrid, which is shown in Figure 20. All four ports of the ring hybrid have a characteristic impedance  $Z_0$  (in most cases  $50\ \Omega$ ). The characteristic impedance of the ring is  $Z_0\sqrt{2}$ . The spacing between ports 2 and 4 is  $3\lambda_g/4$  and the spacings between all other adjacent ports are  $\lambda_g/4$ . When the power is applied to any of the ports, it is equally divided between the two adjacent ports. The remaining port is isolated, because the longer signal path introduces a phase reversal and the signals are effectively cancelled. For example, if the RF signal is applied to port 1, it is equally divided between ports 2 and 3. Port 4 is isolated from port 1 and it is therefore selected as the LO port. The LO signal applied to port 4 is also equally divided between ports 2 and 3, but the signals at these ports have  $180^\circ$  phase difference. This property makes the ring hybrid useful in the balanced mixers as the mixer diodes can now be connected to ports 2 and 3.

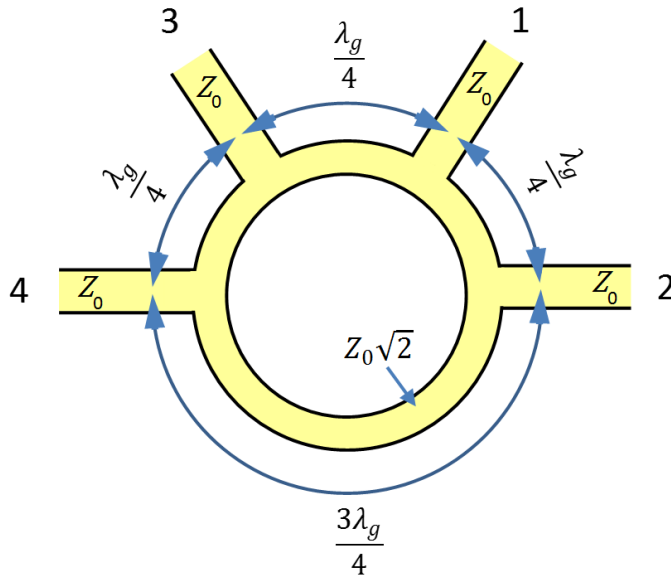


Figure 20. The  $180^\circ$  rat-race hybrid (after [29]).

The passive single-balanced mixer requires a certain power level for the LO signal to turn on the diodes of the mixer. According to the simulations of the directional coupler, tight enough coupling can be achieved for the LO drive of the balanced mixer without a need for a buffer amplifier. However, the balanced mixer has two input responses at frequencies above and below the LO-frequency. Since only one of the side bands contains the signal (the other side band is

called an image frequency), the balanced mixer degrades the signal-to-noise (SNR) ratio of the receiver by approximately 3 dB compared to the image rejection mixer [9]. The RF and LO bands overlap in the FMCW radar and therefore it is not possible to separate the signals by filtering. The image rejection mixer was considered for the receiver, but it turned out that the LO power is not high enough without using the buffer amplifier in the LO chain. The buffer amplifier would increase the power consumption of the altimeter and therefore the idea of using the image rejection mixer was rejected by ESA.

The single-balanced mixer was designed using the microstrip technology on the RT/duroid 6002 substrate. The  $180^\circ$  ring hybrid with RF2M Microwave's MA40126-186 Schottky-barrier diodes were selected for the mixer. A choice of European space qualified Schottky diodes which can be used at high frequencies is very scarce. The selected Schottky diode was the only identified possibility for the Ku-band. The IF output was filtered using butterfly radial stubs. The block diagram of the designed balanced mixer is shown in Figure 21.

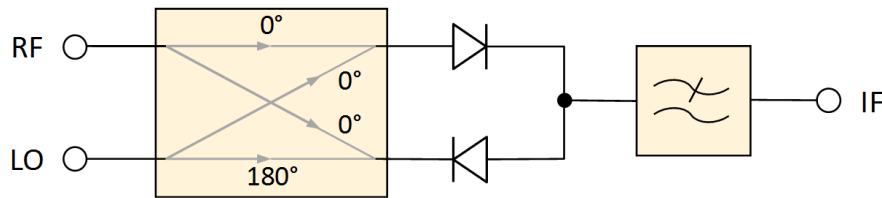


Figure 21. The balanced mixer with  $180^\circ$  hybrid.

The Schottky diodes in the mixer are non-linear devices and therefore the non-linear model of the diode is required to perform accurate simulations. Unfortunately, manufacturers do not usually provide non-linear simulation models of their devices. This was also the case with the selected Schottky diodes. If the non-linear model is not available, the designer has basically two choices: 1) try to make the model from the existing data or 2) perform a small signal analysis and match the impedance of the diodes after the mixer has been manufactured. The first option is quite often a waste of time, because in most cases the model will not meet with the reality and tuning of the circuit will be needed anyway. The second option is preferred in the industry, as it is easy to perform the impedance matching of the diodes during the testing phase of the actual device. The matching can be done by soldering parallel stubs to the ring hybrid when testing the mixer. The dimensions of the stubs can be measured and added to the next layout version of the PCB.

The CST simulation model of the balanced mixer is shown in Figure 22. The ground echo is connected to the RF port 1 and the LO signal to port 4. Schottky diodes are in ports 2 and 3 of the  $180^\circ$  ring hybrid. The diodes are short-circuited from the other ends with radial stubs ( $r = \lambda_g/4$ , angle =  $30^\circ$ ) and ground vias through the PCB substrate. The IF output is taken from port 5, which is at the opposite side of the ring compared to the RF port. Thus, the location of the IF port is symmetric to the diode ports.

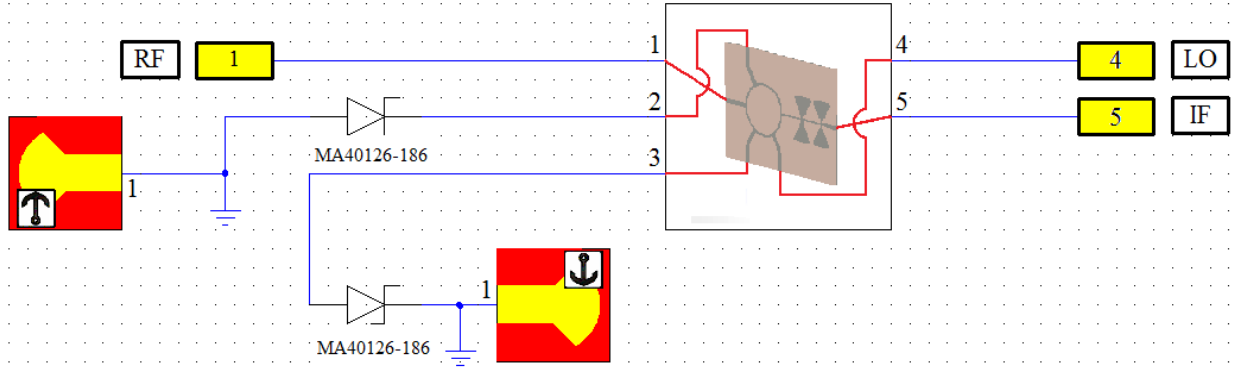


Figure 22. The model of the designed single-balanced mixer.

The dimensions of the  $180^\circ$  ring hybrid were optimized so that the input signals (RF and LO) are equally divided to the Schottky diodes at correct phases. The characteristic impedances of the microstrip lines to ports 1 to 4 are  $50\ \Omega$ . This is achieved with the line width  $w = 0.63\text{ mm}$ . The IF output is connected to the ring with  $w_{IF} = 0.15\text{ mm}$  microstrip line. The characteristic impedance of the ring is  $70.7\ \Omega$  and the corresponding width of the microstrip line is  $w_{ring} = 0.34\text{ mm}$ . The radius of the ring is  $r = 3.6\text{ mm}$ .

The couplings to the diode ports 2 and 3 are shown in Figure 23. The simulated  $S_{21}$  and  $S_{31}$  are both approximately  $-3.2\text{ dB}$  at the center frequency  $13.3\text{ GHz}$ . The isolation between the RF port and the LO port is shown in Figure 24. The leakage is effectively suppressed as it is close to  $-50\text{ dB}$ . The isolation between the RF port and the IF port is shown in Figure 25. The RF-IF isolation (and also the LO-IF isolation) of the design is improved using the radial stub filter in the IF chain. The isolation is approximately  $-55\text{ dB}$ , which is very good.

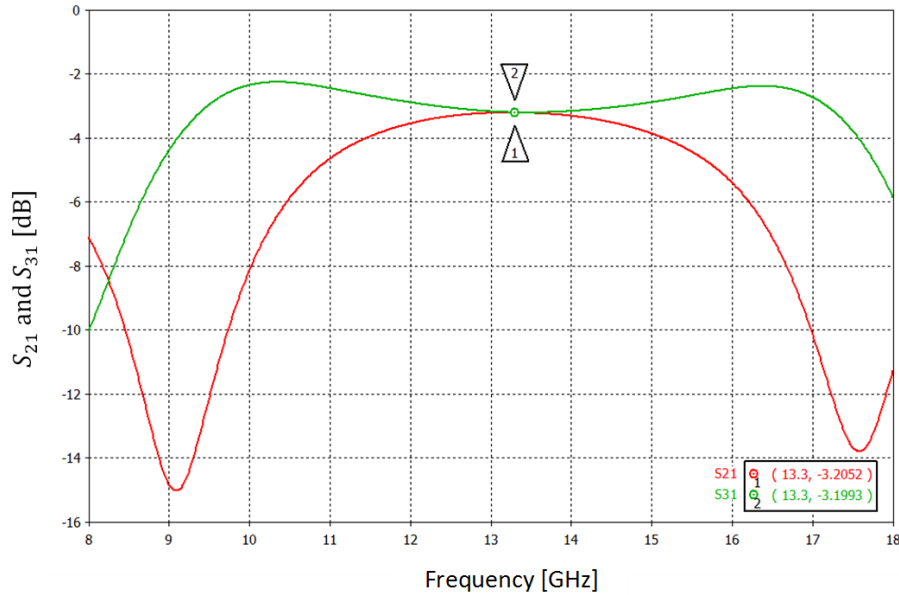


Figure 23. The simulated coupling from the RF port to the diodes (red:  $S_{21}$  and green:  $S_{31}$ ).

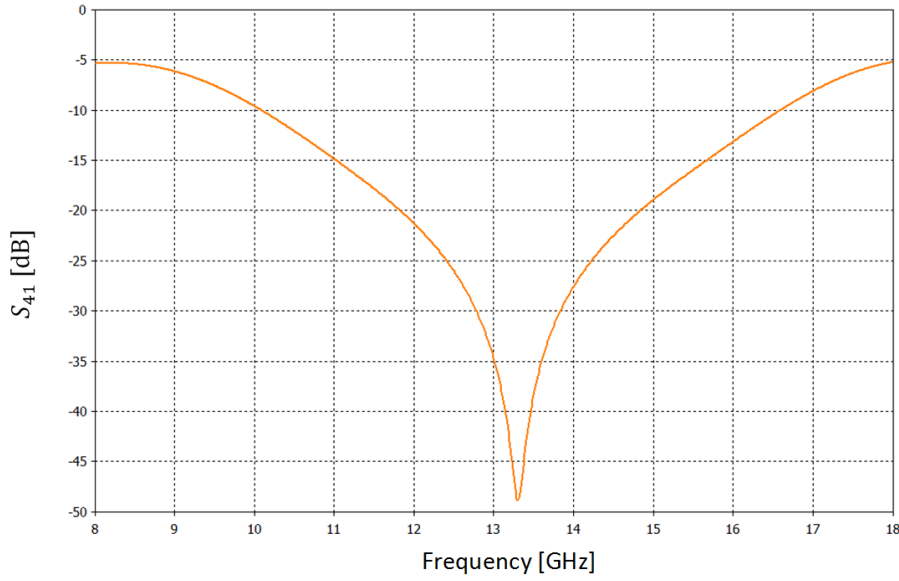


Figure 24. The simulated RF-LO isolation ( $S_{41}$ ) of the mixer.

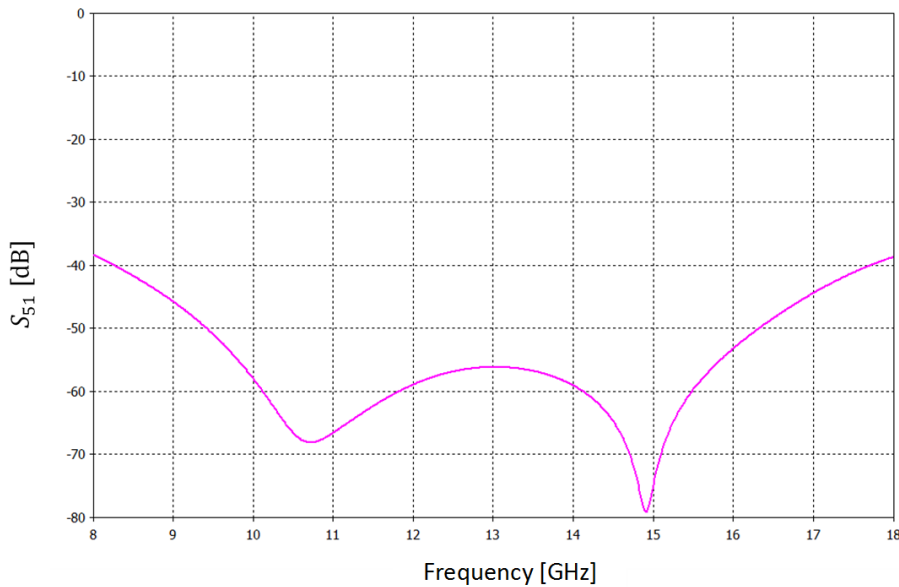


Figure 25. The simulated RF-IF isolation ( $S_{51}$ ) of the mixer.

Very limited data was available for the MA40126-186 Schottky diodes. Therefore, conversion loss of the mixer could not be simulated. The manufacturer stated that approximately 6 dB conversion loss with LO power of 0 dBm has been achieved at X-band. It is expected that the performance will be somewhat lower at 13.3 GHz. The LNA in the front of the mixer has approximately 20 dB gain and therefore it was estimated that as long as the realized mixer has conversion loss  $< 10$  dB it does not contribute too much to the noise figure of the receiver. This will be verified when testing the manufactured mixer. If the performance of the designed passive mixer is not high enough in terms of conversion loss, it might be possible to improve the performance by applying a DC bias to the diodes. This option was designed to the PCB layout of the mixer so that the bias voltage can be fed to the diodes, if it is required.



An enclosure made of aluminum (size: 30.4 x 26.4 x 19 mm<sup>3</sup>) was designed for the mixer and the manufactured PCB was glued to the bottom of the housing. The absorber material (DD-11393) was glued to the lid of the enclosure. The assembled mixer is shown in Figure 26.

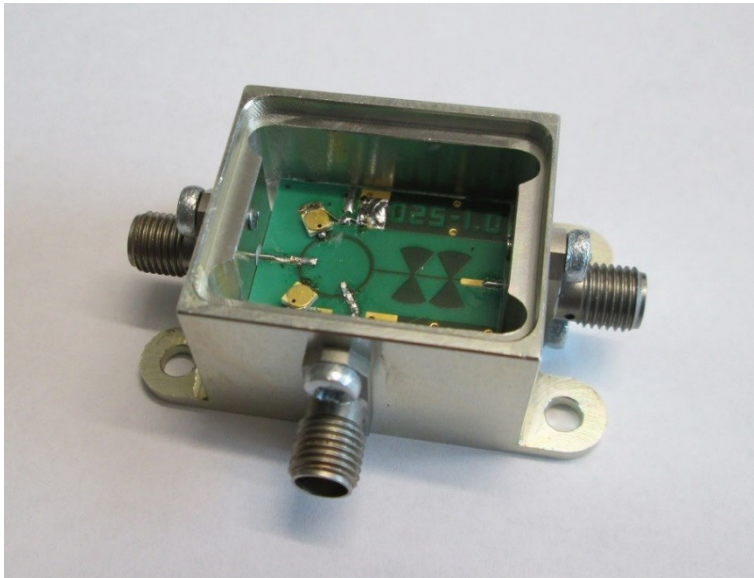


Figure 26. The manufactured balanced mixer.

### 3.2.7 IF chain

The IF chain consists of the Automatic Gain Control (AGC) amplifier, IF filter and comparator. The AGC amplifier is an adaptive system whose gain is varied according to the signal level at the input. The gain is adjusted by feeding the average output signal level back in the AGC amplifier. The input IF signal is weak at high altitudes and the AGC amplifier has high gain then. At low altitudes the received signal is strong and the AGC amplifier has lower gain. This way the range of the input signal levels are kept at the appropriate level for the receiver back-end, i.e., the saturation of the back-end is avoided. A dynamic range requirement is approximately 80 dB as the input signal level of the AGC amplifier can vary between -108 dBm and -30 dBm (see Section 2.6) according to the altitude (from 7 km down to 10 m).

The functional principle of the AGC amplifier is presented in Figure 27. The AGC function is realized with a bipolar junction transistor (BJT) amplifier stage, which has a voltage control at its base.

After the BJT amplifier, the signal is filtered with the IF filter. The bandpass filter is used to suppress all the unwanted mixing products of the mixer output and to obtain only the desired beat frequency. In the servo type FMCW radar the bandwidth can be made small, which improves the SNR of the receiver. The main design parameters of the IF filter are the center frequency  $f_b = 175$  kHz and -3 dB bandwidth of 30 kHz. The bandwidth of the IF filter is quite low and therefore an active topology using operational amplifiers was selected. Originally, the IF filter was placed in front of the AGC amplifier, but after the initial tests it turned out that the available space qualified operational amplifiers were so noisy that they contributed too much to the noise of the whole system. Therefore, the SNR of the receiver was improved by modifying the design architecture and placing the IF filter after the AGC. The IF filter is followed by a fixed gain operational

amplifier. The output voltage is then measured by a Schottky diode peak detector and directed to a feedback path of the gain control. The feedback path consists of a loop amplifier and a loop filter.

The fixed gain amplifier is followed by a voltage comparator. The comparator converts the sinusoidal beat signal to a square wave required by the radar back-end. The IF chain has also an analog IF output before the comparator for basic functional testing of the radar front-end. The detailed design of the IF components was further done by Lic. Sc. (Tech) Kari Lehtinen. The gain of the whole IF chain is approximately 80 dB, when the gain of the AGC amplifier is at the maximum.

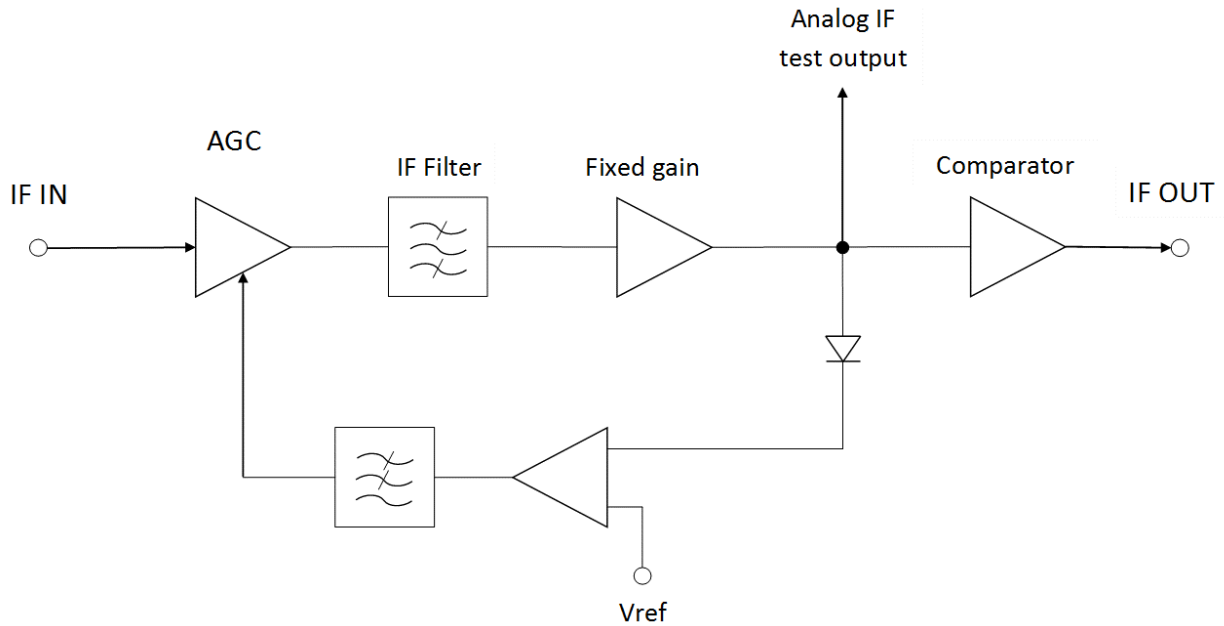


Figure 27. The block diagram of the IF chain (AGC, IF filter and comparator).

### 3.3 Estimated power consumption and mass

An estimated power consumption of the radar front-end module was calculated based on datasheets of each individual component. The power consumption breakdown is presented in Table 7. The total power consumption of the radar front-end is estimated to be 2.44 W, which fulfills the required limit of 2.5 W for the radar front-end. The most power consuming component is the VCO (1170 mW).

The power supply voltages provided by the PSU of the radar back-end are +6 V, -6 V and +15 V. The +5 V and +4 V supply voltages required by the active RF parts (VCO, PA and LNA) must be regulated from the +6 V supply. The voltage regulation consumes approximately 0.5 W in the radar front-end module.

Table 7. The estimated power consumption of the TX/RX module.

Component	Power consumption $P$ [mW]		
	Component	Regulation	Total
VCO ( $V_{CC}=+5V$ )	975	195	1170
PA ( $V_{CC}=+4V$ )	320	160	480
LNA ( $V_{CC}=+4V$ )	320	160	480
AGC ( $V_{CC}=+6V$ )	200	0	200
IF filter ( $V_{CC}=+6V$ )	50	0	50
VCO controller ( $V_{CC}=+12V$ )	60	0	60
<b>Total power consumption</b>	<b>1925</b>	<b>515</b>	<b>2440</b>

An estimated mass was calculated based on the selected parts and the dimensions of the individual component housings. The mass breakdown is shown in Table 8. The estimated mass of the breadboard module is approximately 0.5 kg, which is less than the maximum target mass 0.67 kg.

Table 8. The estimated mass of the TX/RX module.

Component	Mass [g]
VCO	26
PA	29
Directional coupler	51
LNA	29
Mixer	39
EEE parts	20
Electronics PCB	69
Mounting decks	151
D-Sub HD44 connector	13
RF cable harness	75
Wires	10
<b>Total mass</b>	<b>512</b>

### 3.4 Breadboard of the radar front-end

The developed RF components were attached on two aluminum plates (size: 146 x 96 x 2 mm<sup>3</sup>). One plate was used for the transmitter parts (the VCO, PA and directional coupler) and another plate for the receiver parts (the LNA and mixer). The third deck of the radar front-end module is formed by the electronics PCB.

RF interconnections between the individual RF components were done with straight SMA adapters and coaxial cables (Huber+Suhner Suco-Form). The tuning voltage of the VCO is sensitive to an external radio frequency interference (RFI). Therefore, a coaxial cable was used to connect the tuning voltage to the electronics PCB. RF interfaces to the transmitting (TX) and receiving (RX) antennas are 3.5 mm SMA wall mount sockets (ESCC 3402/002 variant 18 from

Radiall [32]). The antenna connectors are located on the long side edge of the radar front-end module.

The temperature transducers and the supply voltages of the active RF components were connected to the electronics PCB by using internal wiring. The wire of size AWG 24 was used. The electrical interface between the radar front-end module and the radar back-end is a 44-pin D-Subminiature (DB-44HD) connector which is soldered directly to the electronics PCB.

A photograph of the constructed radar front-end module is shown in Figure 28. The transmitter is mounted on the top deck, the receiver is in the middle deck and the electronics PCB can be seen at the bottom of the structure. All three decks will be installed in the housing provided by the prime contractor (EFACEC). The housing of the radar front-end module is not shown in the photograph.

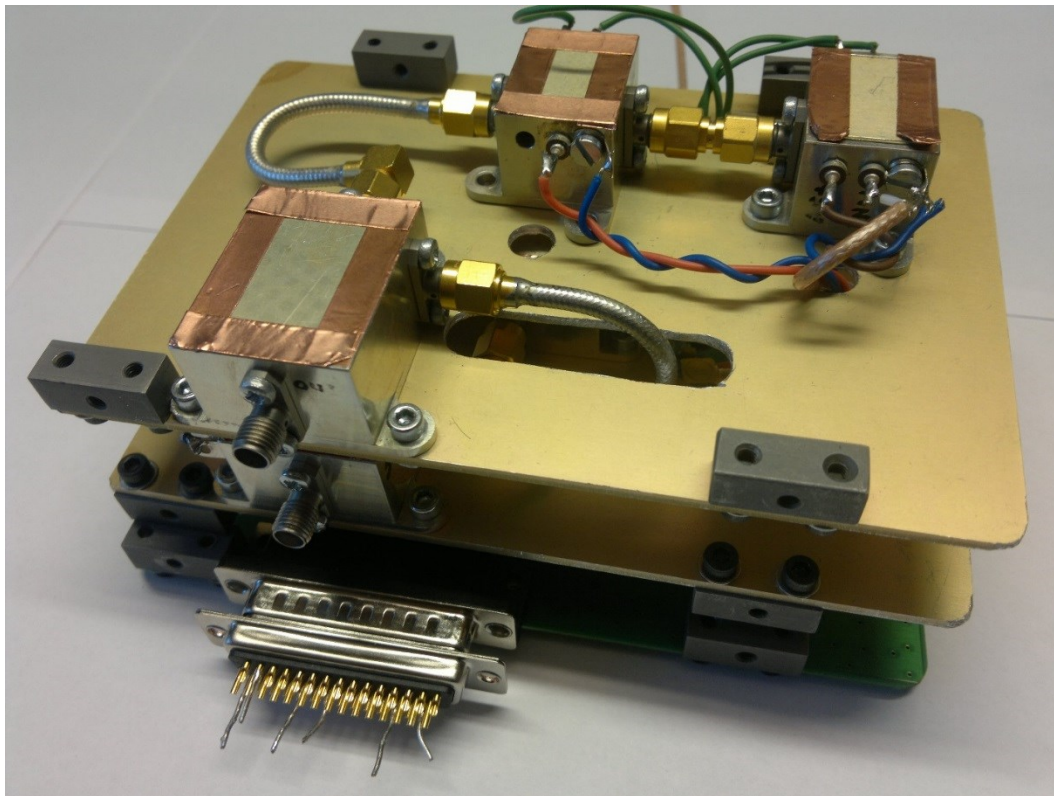


Figure 28. The photograph of the radar front-end module.

## 4. Measurements of functional components

### 4.1 VCO measurements

Three VCO units were manufactured and their performance was verified with measurements. Tuning voltage and power supply inputs of the VCO were connected to a laboratory bench power supply in initial tests. The output frequency was measured with a spectrum analyzer.

It was discovered early on that the tuning voltage of the VCO is sensitive to an external radio frequency interference (RFI). During certain office hours the phase noise of the output signal increased significantly and occasionally the signal had additional spikes. A testing laboratory of Harp Technologies is situated in a crowded office building, where there are multiple wireless RFI sources from various commercial companies. Early mornings and late evenings were identified as quiet hours for testing, but the actual source of RFI was never discovered. A measurement set-up was also improved by using coaxial cables in the inputs of the VCO and a special care was taken to minimize ground loops. However, these measures were not enough to completely remove the sensitivity to RFI from two of the manufactured VCO units. The VCO units were then tested outside the facilities of Harp in quiet RF environment, where the problem disappeared completely.

Although one VCO unit was less sensitive to RFI and was deemed good enough for the breadboard, a design change was decided for the following Engineering Model phase of the project. In the breadboard model, the triangular wave generator is located at the radar back-end. The triangular wave generator will be brought to the radar front-end in the Engineering Model, where all the radar front-end parts will be integrated into the same housing. Also, the VCO controller circuitry will be placed as close as possible to the VCO and proper grounding is ensured in the electronics PCB layout. It is expected that these measures will improve the performance of the VCO.

A behavior of the best VCO unit was characterized in a thermal chamber. The required frequency bandwidth of the radar is 13.25 – 13.35 GHz. At first, five different VCO control voltage values to achieve the required frequency range were measured at room temperature  $T = +20^{\circ}\text{C}$ . The measured voltages are shown in Table 9. The frequency bandwidth is obtained with the control voltage values ranging from 11.79 V to 12.74 V. The values are higher than anticipated from the datasheet of the HMC529 component (see 3.2.2, Figure 12), because the expected values were in the range of 8.5 to 9.5 V. However, according to the manufacturer (Hittite), the performance is in the range of production tolerances. As a consequence, the variation of the tuning voltage must be taken into account in the VCO controller circuit for the Engineering Model. The design cannot be locked based on the measurements performed for the VCO used in the breadboard model.

Table 9. The measured VCO tuning voltages at room temperature.

Frequency	Voltage
13.25 GHz	11.79 V
13.275 GHz	12.02 V
13.3 GHz	12.26 V
13.325 GHz	12.5 V
13.35 GHz	12.74 V

After the VCO performance at room temperature was known, the measurements were repeated over larger bandwidth in five different ambient temperatures (i.e.  $-20^{\circ}\text{C}$ ,  $0^{\circ}\text{C}$ ,  $+20^{\circ}\text{C}$ ,  $+40^{\circ}\text{C}$  and  $+60^{\circ}\text{C}$ ). The measured frequencies as a function of the tuning voltages are shown in Figure 29. The VCO has very linear response over the required bandwidth. The operational temperature range of the Engineering Model will be from  $-40^{\circ}\text{C}$  to  $+60^{\circ}\text{C}$ . It can be estimated from the measured graph that the output frequency of the VCO will shift approximately 100 MHz, when the ambient temperature changes from the low-end to high-end. In order to keep the antenna performance at the optimum, a temperature compensation circuit will be added to the VCO controller in the Engineering Model. In the breadboard model, the temperature compensation was not required.

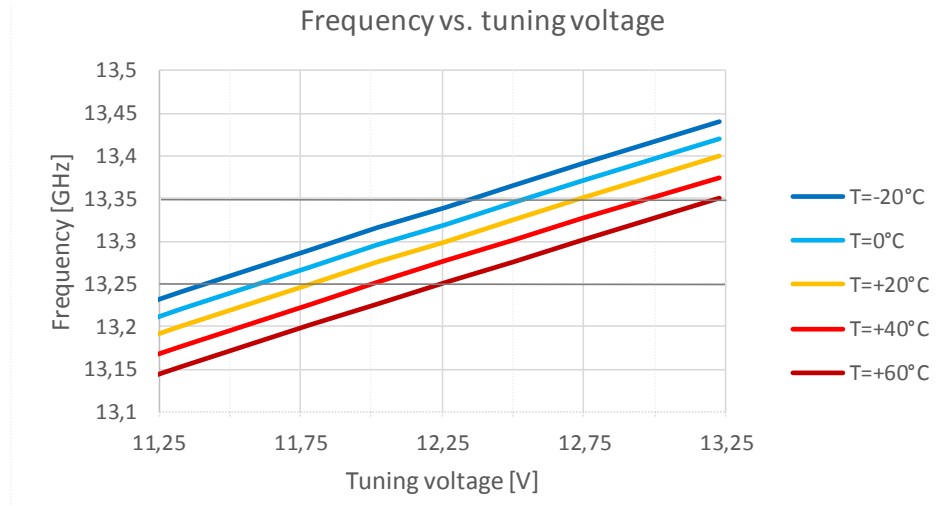


Figure 29. The VCO output frequency at five discrete temperatures as a function of the tuning voltage.

The output power of the VCO was measured at room temperature with a power meter. Results as a function of frequency are shown in Figure 30. The output power is approximately 1 dBm at the center frequency 13.3 GHz. The measured output power is lower than the typical value for the HMC529 component (4 dBm), but it is high enough to drive the PA and thus compliant with the target value. The manufacturer appealed the production tolerances also regarding this issue.

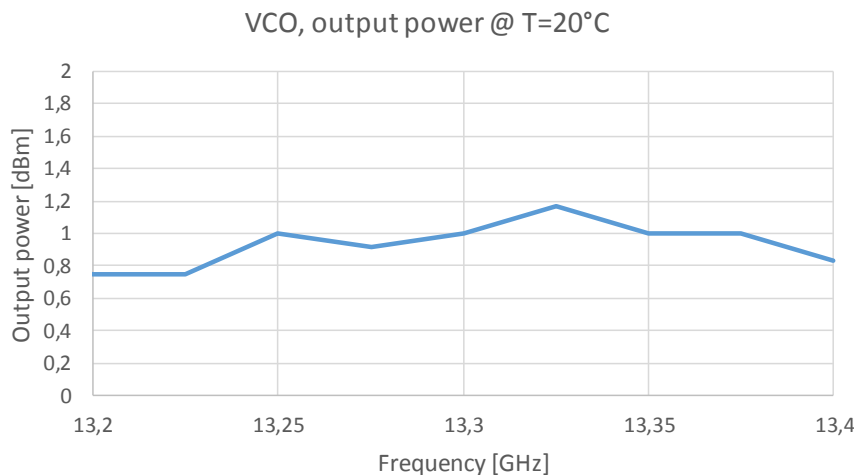


Figure 30. The measured output power of the VCO at room temperature.

## 4.2 VCO controller

The target operating frequency range 13.25 – 13.35 GHz at room temperature is achieved with the VCO tuning voltage range 11.79 – 12.74 V (see Table 9). An authorized frequency band for Earth exploration satellites and space research services is 13.25 – 13.4 GHz [33]. The prime contractor, EFACEC, will test the planetary altimeter during a hot air balloon flight in Portugal. Summer temperature in Portugal tends to be higher than +20°C. Consequently, the operating frequency range of the radar will then shift downwards, because the temperature compensation was not required in the breadboard model. In order to increase the margin to the lower end of the authorized frequency range it was agreed with EFACEC that the tuning voltage shall be shifted upwards to achieve the center frequency of approximately 13.325 GHz at room temperature. The VCO controller circuitry was tuned accordingly.

The output voltage of the VCO controller as a function of time is shown in Figure 31. The input signal in the measurement was 1 kHz triangular wave with -1.5 to +1.5 V peak-to-peak variation. The measured VCO tuning voltage range is 12.03 – 13.06 V. As a result, the range of the VCO output frequency is 13.28 – 13.389 GHz at room temperature.

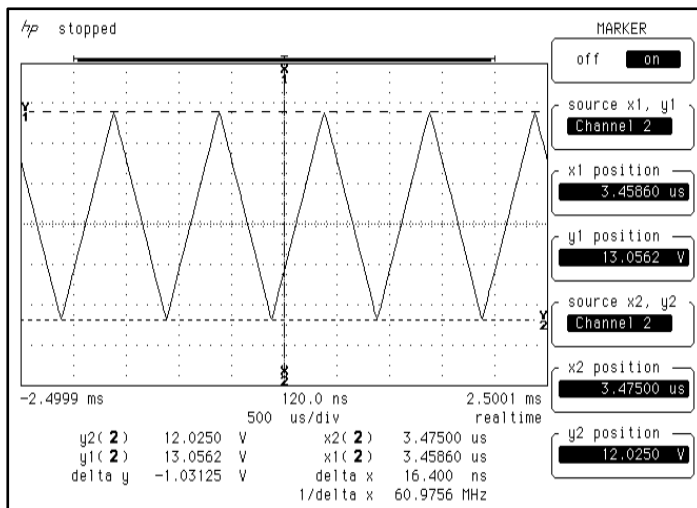


Figure 31. The measured output voltage of the VCO controller as function of time.

## 4.3 S-parameters of RF components

S-parameters of the LNA, PA, directional coupler/isolator and mixer are measured with a vector network analyzer (VNA). Gain, insertion loss, coupling and isolation values are retrieved from the S-parameters.

### 4.3.1 LNA and PA

Four amplifier units based on the UMS CHA3666 component were manufactured. Two units with the best performance in terms of gain and output power were selected as candidates for the LNA and PA. The remaining units were stored as spare parts in case of malfunction during the test campaign of the radar front-end module.



The measured  $S_{21}$  (i.e. gain) of the two amplifier units are shown in Figure 32. The performance of the amplifier units is very similar. The selection of which unit will serve as the LNA and which as the PA was based on the output power measurements performed in following Section 4.4. However, the final amplifier selection is shown in Figure 32 for clarity. The LNA unit shown in green color has 19.6 dB gain and the PA unit shown in red color has 19.2 dB gain at the operating center frequency 13.3 GHz. The performance is compliant with the target value as the typical gain of the CHA3666 component is 19 – 21 dB at 13.3 GHz according to the datasheet [24].

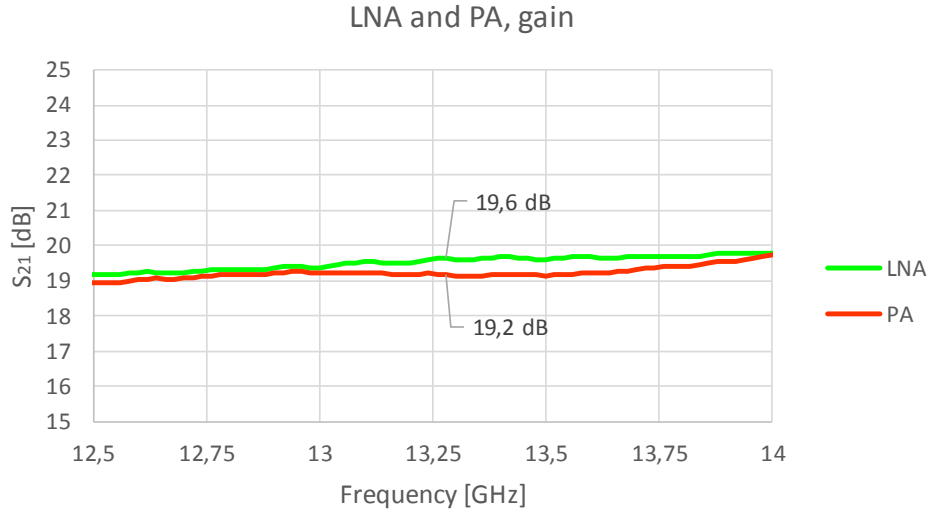


Figure 32. The measured gain of the LNA (green) and PA (red).

The measured input and output reflection coefficients ( $S_{11}$  and  $S_{22}$ ) are shown in Figure 33. The LNA and PA units show similar performance. For both amplifier units,  $S_{11}$  is  $< -20$  dB and  $S_{22}$  is  $< -10$  dB over the operating frequency band 13.25 – 13.35 GHz. The performance of the amplifiers is compliant in terms of the input and output reflection coefficients.

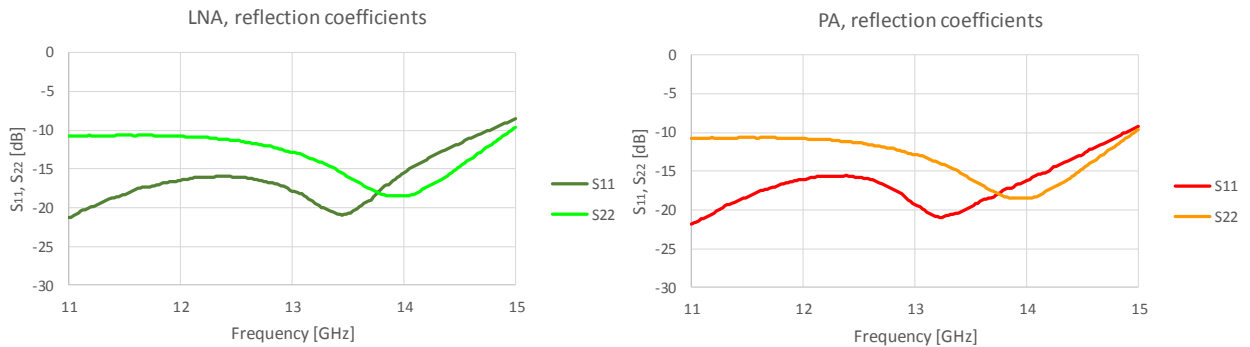


Figure 33. The measured reflection coefficients of the LNA (left graph) and PA (right graph).

#### 4.3.2 Directional coupler/isolator

Two directional coupler/isolator units were manufactured. Both units had very similar performance, but only the measurements of the selected unit are presented in the following figures. The remaining unit was stored as the spare part for the radar.

$S_{31}$  of the directional coupler/isolator was measured with the VNA. The output port to the TX antenna (port 2) was terminated with a  $50 \Omega$  SMA load during the measurement. The measured  $S_{31}$  is shown in Figure 34. The coupling  $C$  of the directional coupler is the absolute value of the



$S_{31}$  (i.e.  $|S_{31}|$ ), and it is 15.5 dB at the operating center frequency 13.3 GHz. The simulated coupling was 10.7 dB at 13.3 GHz (see Figure 16). The difference between the simulated and measured performance is most likely due to the production tolerances of the PCB. The narrow gap ( $s = 0.12 \mu\text{m}$ ) between the coupled lines determines the coupling of the directional coupler. If the gap is wider than specified, the coupling gets worse. It was not required to use a space qualified PCB manufacturer in the breadboarding phase of the project and thus an ordinary manufacturer was used for economical reasons. It is expected that the performance of the directional coupler will improve when higher manufacturing tolerances take place in the Engineering Model of the altimeter.

The output power of the PA is approximately 16 dBm. The coupling  $C = 15.5$  dB leads to higher than 0 dBm LO port power for the mixer. This was considered high enough for the mixer diodes and thus the measured coupling is compliant with the target value.

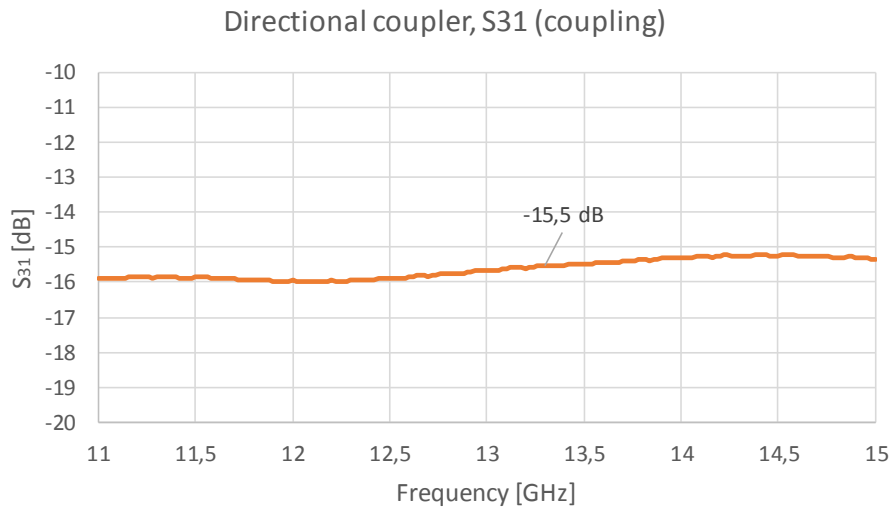


Figure 34. The measured  $S_{31}$  (coupling) of the directional coupler/isolator.

The measured  $S_{21}$  of the directional coupler/isolator is shown in Figure 35. A  $50 \Omega$  termination was installed to port 3 of the coupler during the measurement. The absolute value of  $S_{21}$  is also the insertion loss of the coupler. The measured insertion loss is 1.6 dB at the operating center frequency 13.3 GHz. The simulated insertion loss was 0.7 dB. However, the drop-in isolator NJ1140-07 was not included in the simulations. According to the datasheet of the isolator [28], the isolator contributes approximately 0.8 dB to the total insertion loss value of the manufactured coupler, and therefore the measured insertion loss of the directional coupler/isolator combination is very close to the value expected from the simulations.

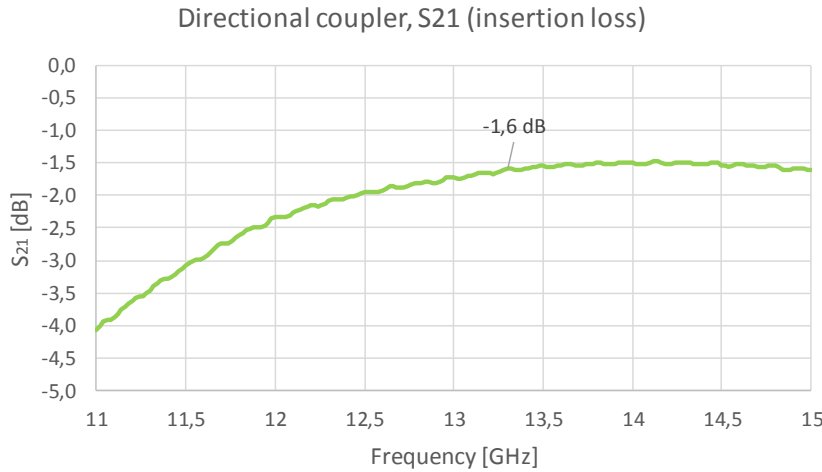


Figure 35. The measured  $S_{21}$  (insertion loss) of the directional coupler/isolator.

The isolations of the directional coupler were retrieved from the S-parameter measurements between ports 2 and 3 of the coupler. Port 2 is the output port to the TX antenna and port 3 is the LO port to the receiver mixer. The isolation from the TX antenna to the LO port is higher than in the opposite direction, because the drop-in isolator contributes to the total isolation.

The measurement results are shown in Figure 36. The isolation from the TX antenna to the LO port is approximately -52 dB at the center frequency, and it is shown in purple color in the figure. In the opposite direction the isolation is approximately -28 dB, and it is shown in blue color in the graph below. This LO-TX direction is the actual isolation of the directional coupler, where only the insertion loss of the isolator contributes to the value. The LO-TX isolation can be compared to the simulated isolation of approximately -22.5 dB (see Section 3.2.4). The reason that the actual measured isolation is better than the simulated isolation is due to the fact that the gap between the coupled lines is wider than specified. The wider gap causes weaker coupling, but at the same time the isolation is improved.

The directivity of the coupler can be retrieved from the difference between the coupling and the isolation. Thus, the measured directivity is approximately  $27.6 \text{ dB} - 15.5 \text{ dB} = 12.1 \text{ dB}$ , which is comparable to the value retrieved from the simulations  $22.5 \text{ dB} - 10.7 \text{ dB} = 11.8 \text{ dB}$ .

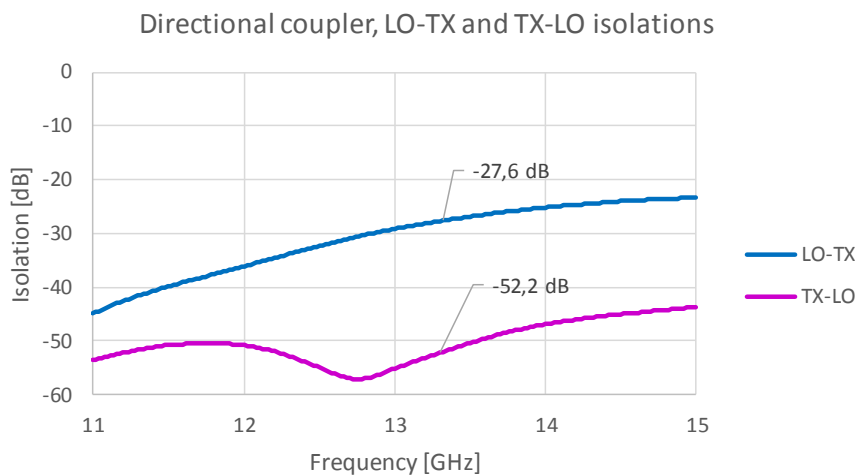


Figure 36. The measured isolations of the directional coupler/isolator (blue: LO port to TX antenna, purple: TX antenna to LO port).

Reflection coefficients of all ports of the directional coupler/isolator were measured to verify that the manufactured coupler does not cause unwanted reflections. The measurements are shown in Figure 37.  $S_{11}$ ,  $S_{22}$  and  $S_{33}$  are all less than -10 dB at the operating frequency band. Therefore, it is expected that the measured reflections are weak enough not to cause harmful oscillations in the radar front-end module.

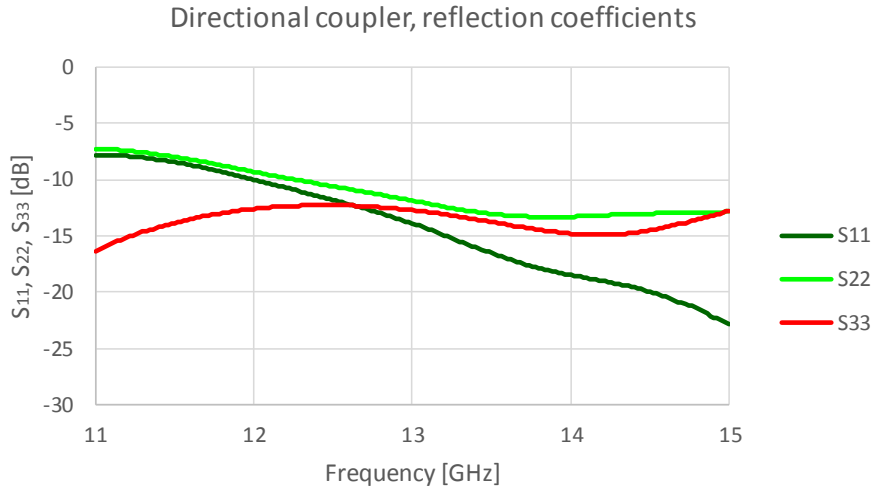


Figure 37. The measured reflection coefficients of the directional coupler/isolator (dark green:  $S_{11}$ , green:  $S_{22}$ , red:  $S_{33}$ ).

#### 4.3.3 Mixer

RF-LO, RF-IF and LO-IF isolations were retrieved from the S-parameter measurements of the manufactured mixer. The third, unused, port was terminated with the 50  $\Omega$  load in each measurement. The measurements were performed for the tuned mixer. The tuning of the mixer was done during the conversion loss measurement of the mixer (see Section 4.5). The isolation results are shown in Figure 38. At the operating center frequency 13.3 GHz, the RF-LO isolation is approximately -30 dB, the RF-IF isolation is -50 dB and the LO-IF is -60 dB. The measured isolations between the different mixer ports are compliant with the target values. The levels of the leaked signals are so low that they are not expected to cause any harmful effects in the radar front-end.

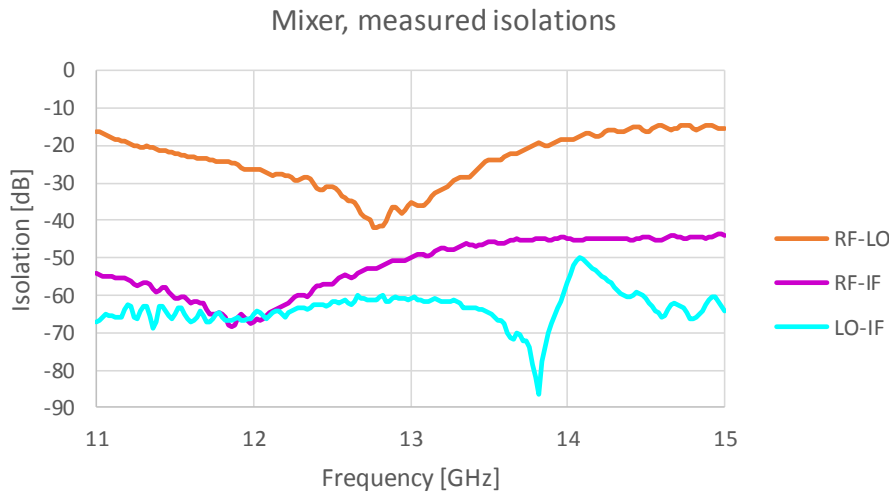


Figure 38. The measured isolations of the mixer (orange: RF-LO, purple: RF-IF and cyan: LO-IF).

## 4.4 PA output power

The output power of the two previously selected CHA3666 amplifier units (see Section 4.3.1) were measured with a power sensor over the frequency band 13.2 – 13.4 GHz. The VCO was installed at the input of the amplifier to provide the input signal power and to simulate the real situation in the final radar front-end module.

The measured output power of the LNA and PA units are shown in Figure 39. The unit with higher output power is selected as the PA for the transmitter. The target output power for the PA is  $P_{out} > 16$  dBm over the operating frequency band 13.25 – 13.35 GHz. Thus, the measurements of the amplifier unit shown in red color are compliant with the target value and this unit is therefore selected as the PA. The other unit, which has slightly higher gain (see Figure 32), but lower output power, is selected as the LNA.

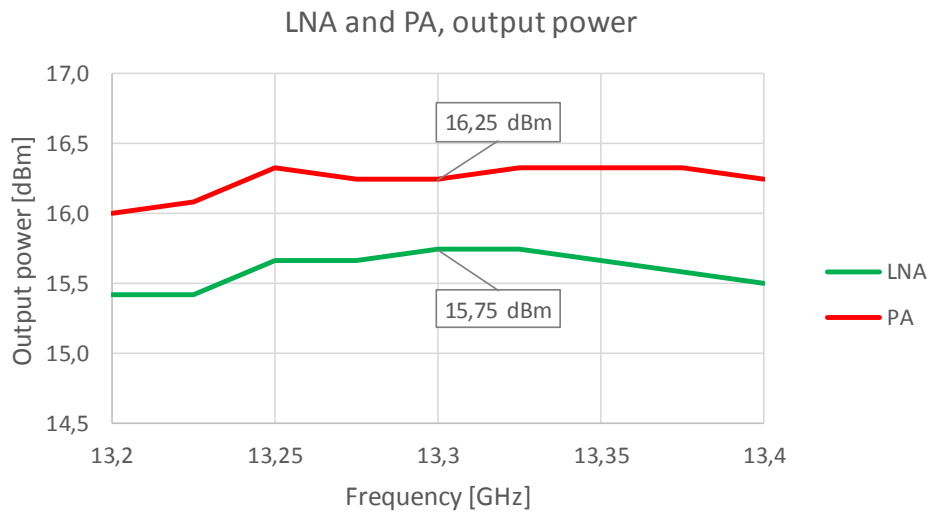


Figure 39. The measured output power of the LNA (green) and PA (red).

## 4.5 Mixer conversion loss

A conversion loss of the mixer was measured with a spectrum analyzer and a power meter. Two constant frequencies were fed to the inputs of the mixer: one to the LO port and one to the RF port. The LO frequency  $f_{LO} = 13.3$  GHz was generated with the HMC529 evaluation card and the signal power was verified with the power meter. The output signal power of the HMC529 evaluation card was measured to be +4.5 dBm at 13.3 GHz. The LO power level range from -1.5 dBm to +4.5 dBm with discrete 1 dB steps was generated by using attenuators at the output of the evaluation card. The RF signal  $f_{RF}$  was generated with a vector network analyzer (VNA) and the power level of the signal was set to  $P_{RF} = -25$  dBm. The RF signal  $f_{RF}$  was adjusted to have 175 kHz (i.e. the center frequency of the IF signal) offset to the LO signal  $f_{LO}$ . Thus, the output frequency  $f_{IF}$  produced in the IF port of the mixer is also 175 kHz.

The Schottky diodes of the mixer were matched during the testing by soldering copper foil stubs to the ring hybrid: one stub to the RF port and one to the LO port. Approximately 1 dB

improvement to the conversion loss was achieved by tuning the mixer. The dimensions of the stubs can be measured and later added to the PCB layout of the Engineering Model.

A power difference between the IF signal and the RF signal was recorded for each discrete LO signal power level. The difference in the power levels is the conversion loss of the mixer, and the measurement results are shown in Figure 40. The actual LO signal power level coming from the directional coupler will be 0 – 1 dBm. Thus, the conversion loss of the mixer is 9 – 9.5 dB in the real use. The conversion loss was also verified to remain constant over the frequency band from 25 kHz to 250 kHz by varying the frequency of the RF signal.

The design goal for the conversion loss was set to <10 dB in Section 3.2.6. Therefore, the measured value fulfills the target. According to the manufacturer of the Schottky diodes, approximately 6 dB conversion loss with 0 dBm LO power has been achieved at X-band. It is highly possible that the given performance is for the single-diode mixer. The LO port power is divided into two diodes in the manufactured single-balanced mixer, and therefore LO power for the diodes is 3 dB less than in the referred case. Also, the utilized center frequency 13.3 GHz is higher. Thus, measured conversion loss of the realized mixer is expectedly somewhat higher. Although the measured value is considered to be sufficient, it would be beneficial to have slightly higher LO signal power to the mixer. The performance can be improved in the Engineering Model of the radar, when tighter coupling from the directional coupler will be achieved with narrower manufactured gap between the coupled lines. It is then possible to increase LO port power up to approximately 4 – 5 dBm.

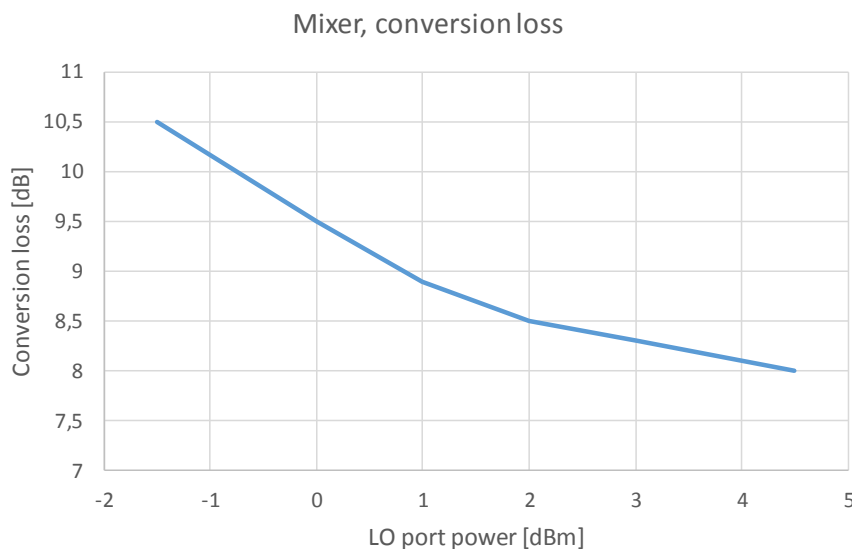


Figure 40. The measured conversion loss of the mixer as a function of the LO port power.

## 4.6 IF chain measurements

### 4.6.1 IF filter

The target for the pass-band of the IF filter is 160 – 190 kHz (i.e. the center frequency 175 kHz with 30 kHz bandwidth). A function generator was used to generate the input signal for the IF filter. The frequency response of the IF filter was then measured with an oscilloscope (frequency

range 100 Hz – 9 kHz) and a spectrum analyzer (frequency range 9 kHz – 2MHz) at room temperature.

The targeted and measured attenuation of the IF filter at different frequency ranges are summarized in Table 10. The measured attenuation values are compliant with the target values except for slightly too high insertion loss in the pass-band (160 – 190 kHz). The frequency response in the pass-band region was further measured in a thermal chamber at three discrete ambient temperatures (-20°C, +20°C and +60°C). The results are shown in Figure 41. It can be seen in the figure that the bandwidth of the filter is slightly narrower than the target bandwidth of 30 kHz. Higher than 3 dB attenuation occurs at the high-end of the pass-band. Narrower bandwidth is not considered critical in the breadboard model and it was not required to tune the IF filter to achieve exact target bandwidth. The tuning of the IF filter can be performed for the Engineering Model of the radar, if required.

Table 10. The targeted and measured attenuation values at different frequency ranges.

Frequency range	Attenuation, target [dB]		Attenuation, measured [dB]
	Min	Max	
0 - 30 Hz	100		> 120
30 - 100 Hz	90		> 120
0.1 - 1 kHz	70		> 120
1 - 10 kHz	50		> 120
10 - 17 kHz	45		> 100
17 - 126 kHz	22		> 21
160 - 190 kHz		3	< 3.6
224 - 1000 kHz	17		> 18
1 - 500 MHz	30		> 57

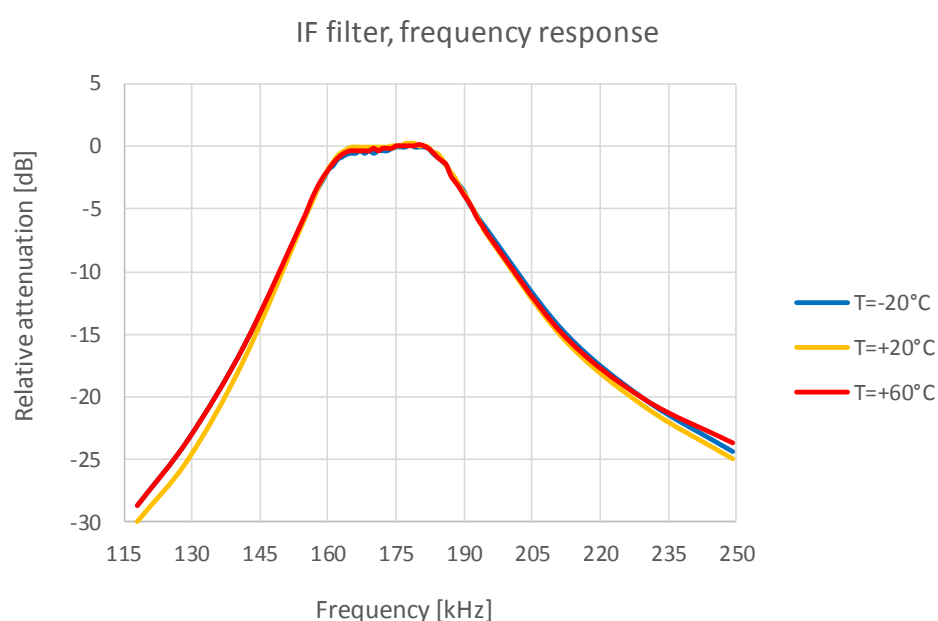


Figure 41. The attenuation of the IF filter in the frequency range 115 – 250 kHz.

#### 4.6.2 AGC amplifier

The gain of the AGC amplifier as a function of input power was measured with a spectrum analyzer in a thermal chamber. A function generator was used to generate a sinusoidal input signal ( $f = 175$  kHz) for the AGC. Figure 42 shows the measured small signal gain in three different ambient temperatures ( $-20^{\circ}\text{C}$ ,  $+20^{\circ}\text{C}$  and  $+60^{\circ}\text{C}$ ). The maximum gain with weak input signals is approximately 80 dB. The gain of the AGC amplifier changes approximately 55 dB as the input power level varies between  $-20$  dBm and  $-110$  dBm and the temperature dependence of the gain is very small. The AGC analog output signal to the comparator is allowed to change more than 20 dB (i.e. to reach the hysteresis threshold level of the comparator with weak signals), which means that the overall dynamic range is over 75 dB. Although the measured dynamic range is slightly less than the design goal of 80 dB (see Section 2.6), the performance is sufficient for the breadboard. The dynamic range can be improved in the Engineering Model by adjusting the component values. Also, the required dynamic range depends on the landing scenario and the dynamic range can be adjusted accordingly. It is not necessarily required that the radar altimeter can adapt to the worst case landing scenario (poorly reflective surface) and the best case scenario (highly reflective surface) at the same time.

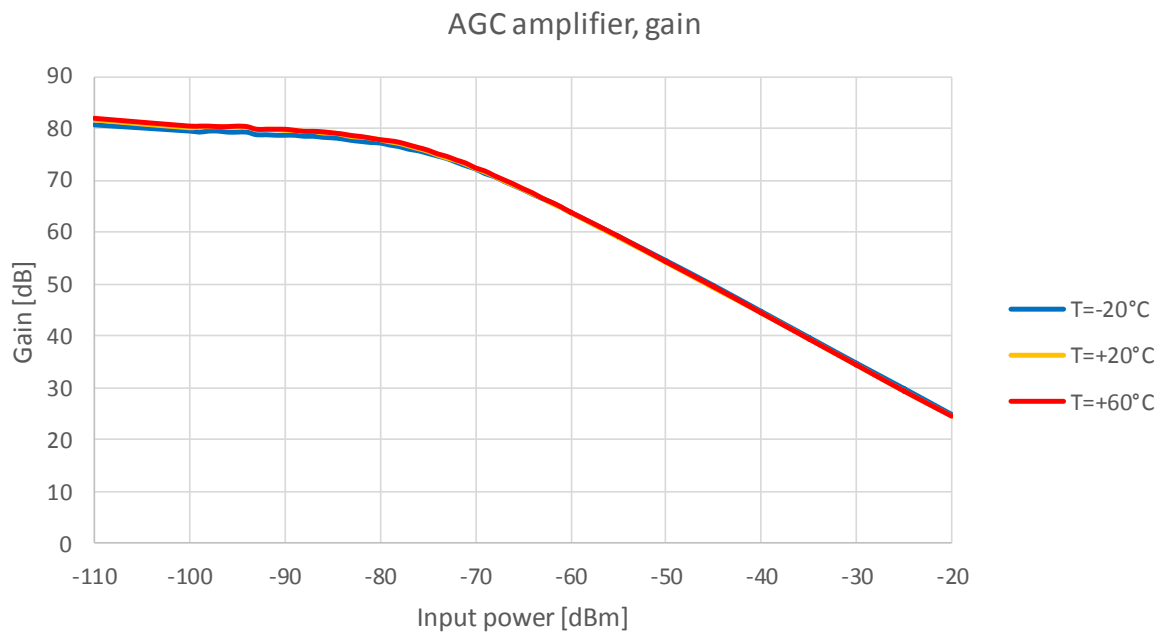


Figure 42. The small signal gain of the AGC amplifier as a function of input power.

## 5. System level tests of the radar front-end

After the performance of each individual component was verified as satisfactory in Chapter 4, the components were attached together to form the breadboard model of the radar front-end. This chapter describes the system level measurements performed for the constructed breadboard.

### 5.1 Transmitter output power

The RF output power of the transmitter was measured in a thermal chamber. A spectrum analyzer and a power meter were used to measure the frequency and power of the output signal across the frequency range 13.2 – 13.4 GHz. The output frequency was unmodulated in the test, i.e., the output frequency of the VCO was set with a constant voltage at the tuning voltage input. Previously measured VCO tuning voltage values (see Section 4.1) were used as the starting point for the test. These results for the VCO component were verified to be valid also for the whole breadboard. The tests for the breadboard were performed at five different ambient temperatures: -20°C, 0°C, +20°C, +40°C and +60°C.

The measurement results of the transmitter output power as a function of the output frequency are shown in Figure 43. The target value for the output power of the transmitter is  $P_{out} > 14$  dBm. The target is fulfilled at the operating frequency range 13.25 – 13.35 GHz except for the ambient temperatures +40°C and +60°C. The reason for the deteriorating performance at higher temperatures is that both the VCO output power and the gain of the PA decrease with increasing temperature. However, even at the ambient temperature +60°C the output power is still approximately 13.5 dBm, which is deemed to be enough for the 7 km measurement distance. In addition, the output power of the radar front-end module is expected to increase, when the RF parts will be integrated into a single housing in the Engineering Model.

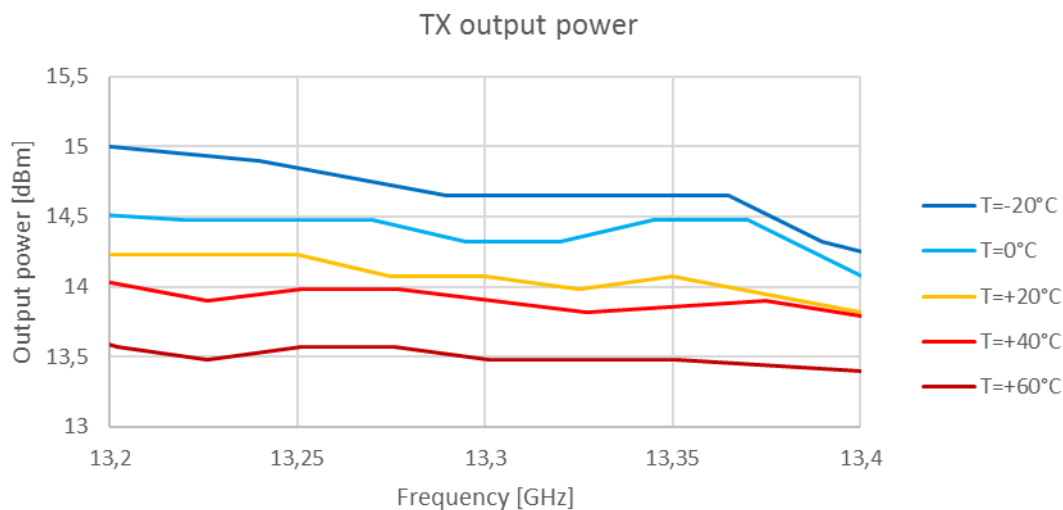


Figure 43. The measured output power of the radar front-end module at five discrete temperatures.



## 5.2 Transmitter sweep bandwidth

The RF output spectrum of the radar front-end was measured at room temperature with a spectrum analyzer. In this test, the VCO was modulated with a triangular wave signal at the VCO tuning input. The triangular wave with a voltage range from -1.5 V to +1.5 V was generated with a function generator and connected to the input of the VCO controller. The input voltage is level-shifted to the range 12.03 – 13.06 V with the current setting of the VCO controller. This setting range leads to approximately 109 MHz sweep bandwidth ( $f_{low} = 13.28$  GHz and  $f_{high} = 13.389$  GHz) at the transmitter output. The test result is shown in Figure 44.

The target value for the sweep bandwidth of the transmitter is 100 MHz. The difference in the measured sweep bandwidth is not critical in the breadboard model, because the VCO in the Engineering Model will require different tuning voltage range anyway. As long as the sweep bandwidth of the breadboard model is close to the target value, the performance is judged sufficient. The actual sweep bandwidth must be used when calculating the altitude in the radar back-end. Accurate characterization of the sweep bandwidth will be performed in the Engineering Model.

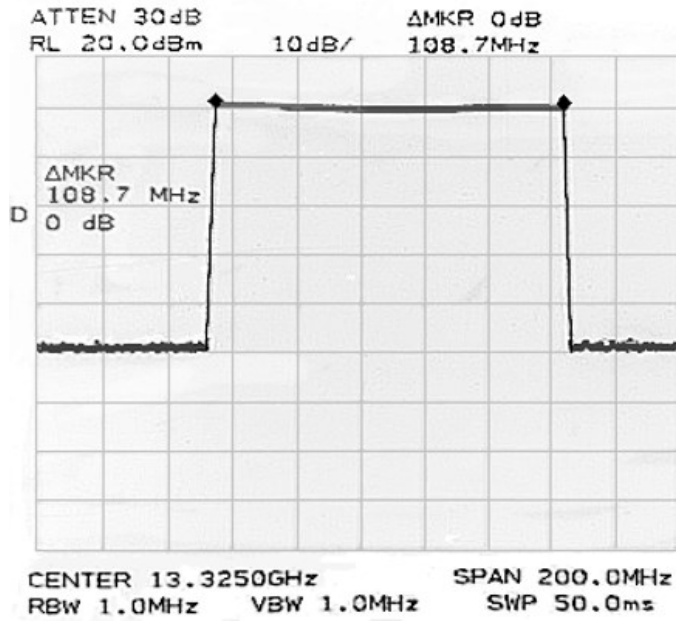


Figure 44. The RF output spectrum with the -1.5 V to +1.5 V triangular wave modulation.

## 5.3 Receiver noise figure

The noise factor ( $F$ ) of the receiver can be determined as the ratio of the available signal-to-noise ratio at the input terminals to the available signal-to-noise ratio at its output [34].

$$F = \frac{S_i/N_i}{S_o/N_o} \quad (5.1)$$

The VCO of the radar front-end was set to provide constant center frequency (13.3 GHz). A signal generator was used to inject a known signal power to the input of the receiver. The frequency of the input signal had 175 kHz offset to the output frequency of the VCO so that the correct beat frequency was obtained at the output of the receiver. The input signal power must be set to a low value (approximately -110 dBm), so that the AGC amplifier of the receiver is providing full constant gain.

The power of the injected input signal was measured with a spectrum analyzer (the resolution bandwidth of the spectrum analyzer was set to 1 kHz). Then the noise level of the signal generator was measured in the absence of the signal. This way, the signal-to-noise ratio (SNR) at the input of the receiver could be determined. The same procedure was used to determine the SNR at the output of the receiver by connecting the spectrum analyzer to the analog IF output of the radar front-end. Now, the noise figure ( $NF$ ) can be calculated from the difference between the input and output SNR.

$$NF = \frac{S_i}{N_i} - \frac{S_o}{N_o} = 6.5 \text{ dB}$$

The used method is rather inaccurate, because the measured signal and noise levels are very low. The measured receiver noise figure can be compared to the theoretical value. The noise factor for the cascaded receiver chain can be calculated from:

$$F_{rec} = F_{LNA} + \frac{F_{mixer} - 1}{G_{LNA}} + \frac{L_{mixer}(F_{IF} - 1)}{G_{LNA}} \quad (5.2)$$

The LNA gain was measured to be  $G_{LNA} = 19.6 \text{ dB}$  and the mixer conversion loss  $L_{mixer} = 9 \text{ dB}$ . For a passive mixer without any gain, the noise figure is almost the same as the conversion loss, i.e.  $NF_{mixer} \approx 9 \text{ dB}$ . The noise figures of the LNA and the IF chain (i.e. AGC amplifier) were not measured, but the noise figures can be estimated from the datasheets of the amplifiers (LNA: CHA3666 and AGC: 2N5551). Thus, the noise figure of the LNA is approximately  $NF_{LNA} = 2 \text{ dB}$  and the noise figure of the IF chain is approximately  $NF_{IF} = 8 \text{ dB}$ . Inserting these values into equation (5.2), solving the receiver noise figure ( $NF_{rec} = 10\log F_{rec}$ ) and adding 3 dB for the noise coming from the image frequency leads to the receiver noise figure  $NF_{rec} = 6.3 \text{ dB}$ . Although the measured noise figure 6.5 dB is considered inaccurate, it is close enough to the calculated value.

The receiver noise figure used to predict the radar range was 6 dB (see Section 2.6, Table 5). The difference in the measured value does not degrade the range much, and the range is still expected to be larger than 7 km even in the case of poorly reflective surface. Therefore, further investigation regarding to the noise figure of the receiver was not required and the performance of the receiver is as expected.

The best solution to improve the noise figure of the receiver would be to use the image rejection mixer instead of the single-balanced mixer. However, this was not an option in this application

due to the power consumption reasons. Therefore, the second best option is to improve the mixer conversion loss in the Engineering Model. This can be achieved by increasing the LO port power coming from the directional coupler.

## 5.4 Power consumption, size and mass

The requirement for the power consumption is  $< 2.5$  W over the full operational temperature range of the breadboard ( $-20^{\circ}\text{C}$  to  $+60^{\circ}\text{C}$ ). The radar front-end module was measured in a thermal chamber at three discrete ambient temperatures:  $-20^{\circ}\text{C}$ ,  $+20^{\circ}\text{C}$  and  $+60^{\circ}\text{C}$ . The power consumption was determined by measuring the operating voltages and currents, while the radar front-end was fully powered on. The AGC amplifier was providing full gain, and thus consuming the maximum amount of power.

The measured values at three operating temperatures are summarized in Table 11. The power consumption is less than 2.5 W over the required temperature range, and thus compliant with the target. The measured value 2.4 W at room temperature is also comparable to the power consumption 2.44 W previously estimated from the datasheets of the individual components.

Table 11. The measured power consumption of the radar front-end.

Temperature	Power consumption	
	Estimated	Measured
$-20^{\circ}\text{C}$	-	2446 mW
$+20^{\circ}\text{C}$	2440 mW	2398 mW
$+60^{\circ}\text{C}$	-	2332 mW

The physical dimensions of the radar front-end module were measured with a caliber. The measured dimensions are  $145.5 \times 95.9 \times 68 \text{ mm}^3$ , and thus compliant with the maximum target dimensions  $150 \times 100 \times 70 \text{ mm}^3$ .

The mass of the radar front-end module was measured with a weight scale. The measured mass is 526 g, and thus compliant with the maximum target mass 0.67 kg.

## 5.5 Functionality tests of the radar front-end

In order to test the functionality of the radar front-end in laboratory conditions, an Electric Ground Support Equipment (EGSE) was developed by Harp Technologies. The EGSE provides 11 different time delays and an adjustable step attenuator to simulate 11 different altitudes and different backscattering coefficients ( $\sigma^0$ ) for all of them. The shortest delay (i.e. 10 m measurement altitude) is implemented using a coaxial cable and all the other delays are generated with SAW filter delay lines.

Table 12 shows the measured average delay values of the EGSE over the operational bandwidth, and the corresponding approximate altitudes. The path loss with the nominal backscattering coefficient  $\sigma^0 = 6 \text{ dB}$  is also presented in the table. The attenuation value can be adjusted  $\pm 15 \text{ dB}$  with the EGSE step attenuator. The theoretical frequency of the modulating signal

to produce the beat frequency 175 kHz in the IF output of the radar front-end is shown in the right column. The measured transmitter sweep bandwidth 109 MHz was used in these calculations.

Table 12. The summary of the EGSE delay configurations.

Delay [ns]	Altitude [m]	Attenuation [dB], $\sigma^0=6\text{dB}$	Triangular wave frequency [Hz]
69	10	54	11634
102	15	57	7870
984	150	77	815.8
984/1086	150/165	77	815.8
1476	220	81	543.9
1967	300	83	408.1
6814	1000	94	117.8
13627	2000	100	58.9
20441	3000	103	39.3
27223	4000	106	29.5
47650	7000	111	16.85

A test setup to measure the performance of the radar front-end with the EGSE is illustrated in Figure 45. All the delay configurations are tested in a thermal chamber at room temperature (+20°C). Two simulated altitudes (10 m and 2 km) are also tested at extreme operational temperatures (-20°C and +60°C).

A function generator is used to generate the modulating triangular wave input for the radar front-end. The theoretical frequency of the modulating signal is retrieved from Table 12 for each delay configuration. Although the EGSE time delays in Table 12 are presented precisely, the actual delays are not known accurately. Especially, the longer delays are not constant over the whole sweep bandwidth (109 MHz), and the delay measurements of the EGSE were noisy due to the high attenuation in the longer delays. Therefore, it is expected that the theoretical modulating frequency values differ slightly from the actual frequencies. The frequency of the triangular wave must be adjusted during testing to obtain the beat frequency 175 kHz at the IF output. If the adjusted modulating frequencies are close to the theoretical values, the radar front-end is working as expected.

The digital and analog IF outputs of the radar front-end are monitored with an oscilloscope. In addition, a spectrum analyzer, a frequency counter and a power meter are used in the basic functionality tests to monitor the analog IF output.

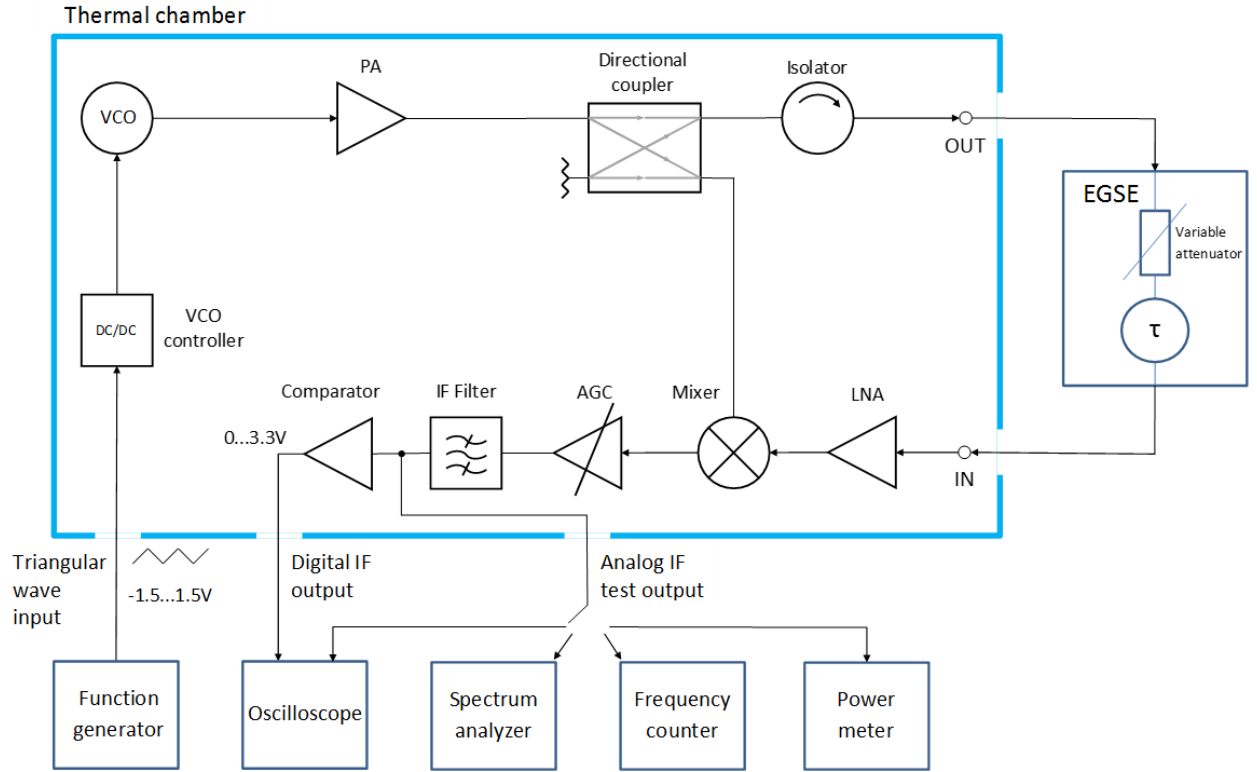


Figure 45. The test setup for the basic functionality measurements of the radar front-end.

The sweep frequencies of the triangular wave generator were adjusted for all delay configurations at nominal temperature ( $T = 20^\circ\text{C}$ ) to obtain the beat frequency  $f_b = 175 \text{ kHz}$ . As the radar front-end was placed in the thermal chamber, test cables at the input and output of the radar introduced an additional delay of 10 ns to the measurement setup. The additional delay was present in all delay configurations except in the 10 m altitude setup. The 10 m delay is created with long coaxial cable, which can be connected directly between the input and output of the radar front-end. The additional delay is significant in the simulated 15 m altitude, where the actual simulated altitude in the measurement setup is approximately 16.8 m. The IF signal waveform and spectral purity were monitored with the oscilloscope and spectrum analyzer connected to the analog IF output. A pure sinusoid signal was observed and spurious frequencies were not detected. A comparison between the theoretical and measured triangular wave frequencies are shown in Table 13. Considering that the time delay values of the EGSE are not exact, the adjusted modulating frequencies are as expected.

Table 13. The adjusted triangular wave frequencies for the VCO tuning input.

Delay [ns]	Approx. altitude [m]	Calculated triangular wave freq. [Hz]	Adjusted triangular wave freq. [Hz]
69	10	11634	11667
112	17	7167	7000
994	150	807.6	810.1
994/1096	150/165	807.6	810.1
1486	220	540.2	541.8
1977	300	406	407.9
6824	1000	117.6	117.9
13637	2000	58.9	57.87
20451	3000	39.3	39.3
27233	4000	29.5	29.5
47660	7000	16.84	16.85

Two simulated altitudes (10 m and 2 km) were further measured by the frequency counter at nominal (+20°C) and at extreme operational temperatures (-20°C and +60°C). The frequency and standard deviation of the IF output signal were measured by averaging over the specified 50 ms refresh period. The results for the 10 m simulated altitude are shown in Table 14. The beat frequency remains stable at different ambient temperatures. The standard deviation of the signal is also very low due to the high signal-to-noise ratio (SNR) in low altitudes.

Table 14. The EGSE 10 m simulated altitude with the modulating frequency 11.667 kHz.

Temperature	Beat frequency	$\Delta f_b$ (standard deviation)
-20°C	175.0 kHz	4 Hz
+20°C	175.0 kHz	7 Hz
+60°C	175.0 kHz	8 Hz

According to Table 12, the nominal attenuation of the EGSE is 100 dB for the simulated 2 km altitude. In order to simulate different backscattering and thus different SNR conditions, the attenuation of the EGSE was varied between 90 to 120 dB while performing the measurements for the 2 km altitude. This test verifies that weak signals can be measured reliably with the radar front-end at different temperatures. The frequency and the standard deviation of the IF output signal were measured with the frequency counter and the refresh period was again 50 ms. The results are shown in Table 15.

The measured beat frequency (with the nominal path loss 100 dB) decreases from 175 kHz at  $T = +20^\circ\text{C}$  to 173.35 kHz at  $T = -20^\circ\text{C}$  and increases to 175.8 kHz at  $T = +60^\circ\text{C}$ . A possible explanation for the behavior is that the output frequency sweep bandwidth of the radar front-end changes slightly with temperature. Also, as the output frequency range of the radar front-end drifts with changing temperature, the downconverted EGSE signal for the SAW delay line filter shifts

away from the center of the filter. Consequently, the actual time delay changes. The temperature compensation was not required in the breadboard and therefore the observed change in the beat frequency is acceptable. It is concluded that the output sweep bandwidth must be characterized accurately over the required operational temperature range to further improve the range accuracy in the Engineering Model. The possible change in the transmitter sweep bandwidth can be compensated in the radar back-end processor.

The beat frequency remains stable with the EGSE attenuation from 90 dB to 110 dB. The measured beat frequency and the standard deviation increase when the attenuation is increased to 120 dB. The received signal is so weak and the SNR so poor that the performance of the radar front-end is approaching its limit. However, the signal is still detected although the range accuracy of the radar has deteriorated. Improving the phase noise performance of the VCO in the Engineering Model is also expected to improve the detectability of the received signal.

The design target for the accuracy of the beat frequency was set to  $\Delta f_b/f_b < 0.23\%$  in Section 2.3.2. This means that the standard deviation of the beat frequency ( $\Delta f_b$ ) must be less than 400 Hz, if the beat frequency  $f_b$  is 175 kHz. The requirement is fulfilled in all measured cases even with very poor signal-to-noise ratios. In order to fulfil the range accuracy requirement 0.33%, also the error in the sweep bandwidth must be  $\Delta B/B < 0.23\%$  (i.e.  $\Delta B < 250$  kHz, if  $B = 109$  MHz). The actual sweep bandwidth and its standard deviation will be fully characterized only after the temperature compensation circuit is added to the design in the Engineering Model. However, it is anticipated that achieving the required accuracy for the sweep bandwidth is not difficult although the measurement method itself will be very time-consuming task.

Table 15. The EGSE 2 km simulated altitude with the modulating frequency 57.87 Hz.

Temperature	Beat frequency	$\Delta f_b$ (standard deviation)
-20°C:		
L = 90 dB	173.35 kHz	99 Hz
L = 100 dB	173.35 kHz	100 Hz
L = 110 dB	173.45 kHz	120 Hz
L = 120 dB	174.8 kHz	207 Hz
+20°C:		
L = 90 dB	175.0 kHz	102 Hz
L = 100 dB	175.0 kHz	104 Hz
L = 110 dB	175.0 kHz	105 Hz
L = 120 dB	175.5 kHz	216 Hz
+60°C:		
L = 90 dB	175.8 kHz	105 Hz
L = 100 dB	175.8 kHz	105 Hz
L = 110 dB	175.8 kHz	109 Hz
L = 120 dB	178.0 kHz	290 Hz

The IF signal waveform was measured from the digital IF output with the oscilloscope. The radar back-end processor requires CMOS logic level signals (i.e. a low value 0 – 0.8 V and a high value 2 – 3.3 V). The square wave produced by the comparator must also represent the same beat frequency as the sinusoidal IF signal before the comparator. The measurement showing the voltage levels of the square wave is shown in Figure 46. The measured logic low is 0.2 V and the logic high is 3.1 V, and thus the digital IF voltage levels are compliant with the target. The square wave is also representing the beat frequency correctly.

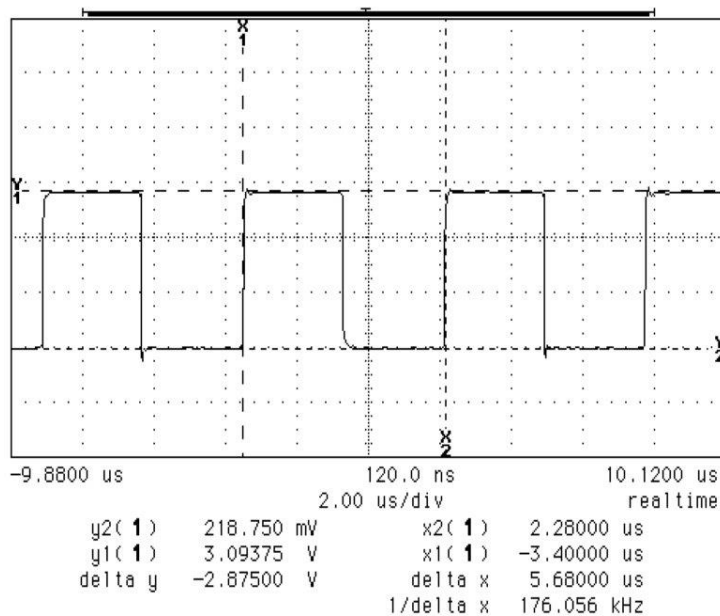


Figure 46. The IF signal waveform in the digital IF output.

The amplitude and frequency of the analog IF signal drop momentarily to zero at every turning point of the triangular modulation. The turning point in the analog beat frequency can be seen in Figure 47.

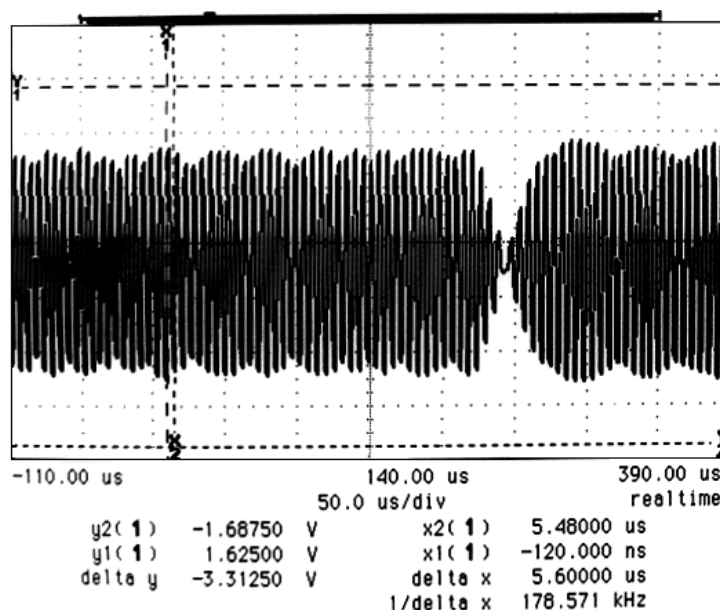


Figure 47. The effect of the triangular wave turning point on the beat frequency.



Figure 48 shows a closer view of the analog and digital IF output signals and what happens in the digital IF signal when the analog signal disappears momentarily. This example was performed with the simulated 10 m altitude of the EGSE and the analog and digital IF outputs were monitored with the oscilloscope. The lower signal (channel 1 of the oscilloscope) in the figure shows the analog IF signal and the higher signal (channel 2) shows the respective digital IF signal. As the analog IF signal disappears momentarily, the digital IF signal stays at the high value. Depending on the phase of the analog signal, the digital output may also stay at the low value during the transition. The radar back-end processor calculates the number of square wave pulses received during the refresh period (50 ms) and retrieves the beat frequency from it. If the phenomenon seen in Figure 48 is not taken into account, a systematic error in the calculated beat frequency may occur.

The worst case scenario happens if the threshold levels of the comparator are not set correctly. In that case, even very weak analog signal may be enough to change the state of the digital signal during transition period, and as a consequence an additional short square wave pulse appears. At the lowest 10 m altitude (where the modulating frequency is 11.67 kHz), the calculated beat frequency would change from the actual 175 kHz to 186.67 kHz. Thus, there is an absolute error of approximately 0.7 m in the measured altitude. At higher altitudes the relative error decreases, because the modulating frequency is then lower. It is concluded that special care must be taken when testing and tuning the Engineering Model of the altimeter to remove systematic errors in the altitude extraction.

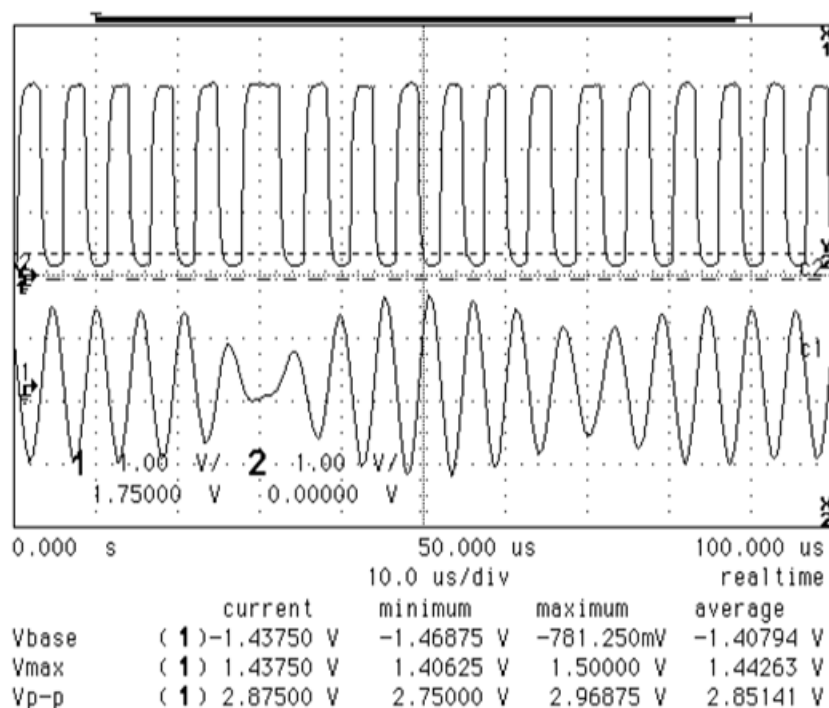


Figure 48. The analog and digital beat frequencies in the outputs of the radar front-end. Channel 1 (lower) is the analog IF output (1 V/div, offset 1.75 V) and channel 2 (higher) is the digital IF output (1 V/div, offset 0 V).

## 6. Conclusions

The European Space Agency has identified a demand for small landers in upcoming scientific Mars missions. Therefore, size, mass and power consumption of all necessary sensors onboard the lander have to be minimized. These drastic requirements apply also to an altimeter sensor, which is used to measure a ground distance during descent and landing.

A development philosophy in a space project is to prove first a feasibility of chosen technology with a breadboard model. Commercial-of-the-shelf (COTS) components, which have space qualified equivalents, can be used in the breadboard model. If the operational requirements are fulfilled with the breadboard, the project can advance to the Engineering Model and finally to the Flight Model.

The development of the breadboard model of the radar altimeter front-end was described in this thesis. Pulse and FMCW radars have strong space heritage in planetary exploration missions. Both technological choices were assessed and the FMCW radar technology was selected for further development. The radar is required to measure the ground distance reliably from the 7 km altitude down to 10 m. As the power consumption requirement for the radar front-end is only 2.5 W, fulfilling the maximum range requirement with the pulse radar was seen too problematic.

A choice of operational frequency in this project depends mainly on the maximum allowed size of the radar and the availability of European space qualified components. Ku-band frequency was evaluated to be the most suitable for this application. In order to test the radar altimeter on Earth, an authorized frequency band was selected leading to the operational center frequency 13.3 GHz with 100 MHz sweep bandwidth. The servo-type FMCW radar technology, where the ramp rate of the frequency sweep is constantly modified, was chosen in order to improve the signal-to-noise ratio of the receiver. The beat frequency is kept constant at 175 kHz by adjusting the ramp rate. The IF bandwidth of the receiver is 30 kHz, which ensures that the anticipated Doppler shifted frequencies fall within the IF band.

The Hagfors model was used to estimate the radar backscattering from the ground surface. The Hagfors model usually shows good agreement with real measurement data of planetary objects. Based on the published surface parameters for Mars, three different landing scenarios were investigated: poorly reflective, typical, and highly reflective surfaces.

System parameters, such as the transmit power, antenna gain and receiver noise figure, were estimated from the functional requirements for the altimeter. Using the assumed parameters, the maximum predicted range of the FMCW radar was analysed for the poorly reflective and typically reflective cases. The analysis revealed that approximately 13 dBm transmit power is required to fulfil the range requirement in the poorly reflective measurement conditions. The system parameters used in the range prediction were set as the target values for the radar design. These target values can be improved, if it is noticed during the design phase that the functional requirements (especially power consumption) have margin to do it.

A system level design of the FMCW radar front-end was performed and technical realisation for each functional component was chosen. The individual components were then designed in to their own housings in order to measure and tune the components before assembling the breadboard

model. The manufactured VCO component showed some sensitivity to RFI, which implied a design change for the following Engineering Model. The triangular wave generator is currently located in the radar back-end and it will be brought to the radar front-end in the EM. This will improve the performance of the VCO. The PA and LNA were based on the same design, because it was estimated that the output power of the LNA component is high-enough for the transmitter. The selected component has also very low power consumption, which is an important factor in this planetary altimeter application. Tight coupling required for the directional coupler causes challenges in production. The performance can be improved, if the gap between the coupled lines is etched accurately. A passive, single-balanced structure was chosen for the mixer. Using this structure is beneficial in terms of power consumption, but it degrades the SNR of the receiver approximately 3 dB compared to the image rejection mixer.

After the performance of the individual components had been verified, the breadboard model of the radar front-end was constructed. The breadboard consists of three decks, which are assembled in the housing provided by the prime contractor, Efacec.

The mass of the manufactured radar front-end is approximately 0.5 kg and the power consumption is less than 2.5 W. The output power of the transmitter is approximately 14 dBm and the output frequency range is 13.28 – 13.389 GHz at room temperature. These values are temperature dependent, but temperature compensation will be implemented in the Engineering Model. The noise figure of the receiver was measured to be approximately 6.5 dB.

A final verification of the radar front-end was done with an Electric Ground Support Equipment. The EGSE simulates 11 different altitudes by introducing a time delay and attenuation to the transmitted signal. Different backscattering conditions can also be inspected by adjusting the attenuation value of each simulated altitude. The performance of the radar front-end was satisfactory in all simulated altitudes. A disappearance of the beat frequency during the turn periods of the triangular wave may cause systematic error in the calculated beat frequency. This can be solved by signal processing techniques. If necessary, a blanking signal can be generated from the analog IF signal. It can be used to discard the non-informative parts of the beat frequency.

The developed breadboard model fulfils the functional requirements for the radar altimeter. The project can continue to the next phase, the Engineering Model. Integrating the RF components in the same housing and introducing some minor changes to them will further improve the performance of the radar front-end.

## References

- [1] Assessment and Bread-boarding of a Planetary Altimeter (ABPA), Statement of Work, Issue 2.0, ABPA-SoW-ECN-20101026, European Space Agency, December 6, 2010.
- [2] G. Brooker, *Introduction to Sensors for Ranging and Imaging*, SciTech Publishing, 2009.
- [3] V. Rosmorduc et al, *Radar altimetry tutorial*, ESA/CNES Publication, Issue 3a, June 2018.
- [4] Honeywell, "Honeywell HG8500 Series Radar Altimeter," datasheet, DFOISR # 03-S-1426, dated 13.6.2003.
- [5] B. D. Pollard and C. W. Chen, "A Radar Terminal Descent Sensor for the Mars Science Laboratory mission," *Proceedings of the 2009 IEEE Aerospace Conference*, 2009.
- [6] N. Hughes, "Story of Huygens radar altimeter," *Avaruushuotain*, pp. 14-18, 4/2006.
- [7] R. Trautner et al, "FMCW radars for entry probes and landers: Lessons learned from the Huygens radar altimeter," *Proceedings of the 3<sup>rd</sup> International Workshop on Planetary Probes*, published as ESA-SP 607, 2005.
- [8] J. Griffiths, *Radio Wave Propagation and Antennas: An Introduction*, Prentice-Hall International, 1987.
- [9] M. Skolnik, *Radar Handbook*, 3<sup>rd</sup> edition, McGraw-Hill, 2008.
- [10] F. E. Nathanson, *Radar Design Principles*, 2<sup>nd</sup> edition, SciTech Publishing, 1999.
- [11] T. Hagfors, "Backscattering from an undulating surface with applications to radar returns from the Moon," *Journal of Geophysical Research*, vol. 69, no. 18, pp. 3779-3784, 1964.
- [12] B. A. Campbell, *Radar Remote Sensing of Planetary Surfaces*, Cambridge University Press, 2002.
- [13] B. A. Campbell and M. K. Shepard, "Coherent and incoherent components in near-nadir radar scattering: Applications to radar sounding of Mars," *Journal of Geophysical Research*, vol. 108, no. E12, 6-1 – 6-8, 2003.
- [14] R. A. Simpson, "Spacecraft studies of planetary surfaces using bistatic radar," *IEEE Transactions on Geoscience and Remote Sensing*, vol. 31, no. 2, pp. 465-482, 1993.
- [15] D. E. Smith et al, "Mars Orbiter Laser Altimeter: Experiment summary after the first year of global mapping of Mars," *Journal of Geophysical Research*, vol. 106, no. E10, pp. 23,689-23,722, 2001.
- [16] International Telecommunication Union, "Radio Regulations: Articles," vol. 1, 2008.
- [17] C. Ho, N. Golshan and A. Kliore, *Radio Wave Propagation Handbook for Communication on and Around Mars*, Jet Propulsion Laboratory Publication 02-5, 2002.

- [18] J. D. Kraus and R. J. Marhefka, *Antennas for All Applications*, 3<sup>rd</sup> edition, McGraw-Hill, 2003.
- [19] A. Räisänen and A. Lehto, *Radiotekniikka*, 7. painos, Otatieto Oy, 1996.
- [20] F. T. Ulaby, R. K. Moore and A. K. Fung, *Microwave Remote Sensing, Active and Passive, Volume II*, Artech House, 1982.
- [21] D. C. Schlerer, *MTI and Pulsed Doppler Radar with MATLAB*, 2<sup>nd</sup> edition, Artech House, 2010.
- [22] Rogers Corporation, “RT/duroid 6002 High Frequency Laminates,” datasheet, 1.6002.
- [23] Hittite Microwave Corporation, “MMIC VCO w/ half frequency output & divide-by-4, 12.4 – 13.4 GHz,” datasheet, v04.0811.
- [24] United Monolithic Semiconductor, “5.8 – 17 GHz Low Noise Amplifier,” datasheet, DSCHA3666-QAG8108, April 17, 2008.
- [25] R. K. Mongia, I. J. Bahl, P. Bhartia, and J. Hong, *RF and Microwave Coupled-Line Circuits*, 2<sup>nd</sup> edition, Artech House, 2007.
- [26] A. Podell, “A high directivity microstrip coupler technique,” *IEEE MTT-S International Microwave Symposium Digest*, pp. 33-36, May 1970.
- [27] European Cooperation for Space Standardization, “Space product assurance – Design rules for printed circuit boards,” ECSS-Q-ST-70-12C, July 2014.
- [28] Cobham Microwave, “Dropin isolator clockwise version 13200 – 13400 MHz,” datasheet for NJ1140-07, May 11, 2010.
- [29] S. A. Maas, *Nonlinear Microwave and RF Circuits*, 2<sup>nd</sup> edition, Artech House, 2003.
- [30] S. A. Maas, *Microwave Mixers*, 2<sup>nd</sup> edition, Artech House, 1993.
- [31] L. E. Larson, *RF and Microwave Circuit Design for Wireless Communications*, Artech House, 1996.
- [32] European Preferred Parts List, Issue 23, 21.6.2013.
- [33] International Telecommunication Union, “Assessment on use of spectrum in the 10-17 GHz frequency band for the GSO fixed-satellite service in Region 1,” Report ITU-R S.2365-0, 09/2015.
- [34] H. T. Friis, “Noise figures of radio receivers,” *Proceedings IRE*, vol. 32, no. 7, pp. 419-422, July 1944.